Spatially Resolved Absorption Spectroscopy of NO in Shock Tube Experiments using an Ultraviolet Tunable Modeless Laser

Maïlys T. B. Buquet*, Benjamin A. O. Williams†, Paul Ewart‡, Matthew McGilvray§, Justin Clarke¶, Luca Di Mare‖
and Tobias Hermann**
Oxford Thermofluids Institute, University of Oxford, Southwell Building , Osney Mead, OX2 0ES Oxford, UK.

Shock tube experiments are conducted in the Oxford T6 Stalker Tunnel utilising a 226 nm bespoke modeless laser for nitric oxide absorption spectroscopy. The laser is expanded into a laser sheet to spatially resolve absorbed light behind the shock wave. Each laser pulse comprises two discrete wavelength ranges, which can be independently tuned within the 224–227 nm range. Nitric oxide (NO) absorption lines are targeted to compare experimentally measured absorbance to NESS–NEQAIR simulations at the nominal experimental conditions and infer number densities through a simple least-squares minimisation. The T6 Stalker facility is used to drive shocks in the 3.3–6.5 km.s^{-1} velocity range, with post-shock pressures varying between 35.8 and 150.7 kPa. The collection optics used for imaging were developed and optimised for VUV emission spectroscopy and designed as a telecentric system. Their performance and resolution are briefly presented in this paper.

I. Introduction

During atmospheric entry, flight vehicles experience extreme heat flux on their surfaces due to the high enthalpy of the surrounding flow field. To withstand these thermal loads, thermal protection systems (TPS) are employed. However, current TPS designs are significantly oversized, resulting in high mass that restricts vehicle performance and limits payload capacity. A major contributor to this overdesign is the uncertainty associated with thermochemical non-equilibrium, which plays a critical role in determining surface heat flux, shear stress, gas radiation, and overall flow field behaviour. Non-equilibrium arises when flow velocities are comparable to the characteristic timescales of chemical reactions and excitation processes.

Advancing the design of hypersonic vehicles and re-entry capsules requires improved predictive capabilities for non-equilibrium flows. Ground-based experiments are used to replicate flight-like conditions, enabling focused investigation of key flow characteristics. A widely used canonical set-up is the shock tube, in which a normal shock wave transiently propagates through a straight tube [1–5]. The shock velocity reflects that of the relevant flight scenario, while the initial test gas density and composition match the atmospheric freestream encountered by the vehicle during entry. Despite being influenced by several facility-specific artefacts [6–8], shock tubes capture one of the most fundamental fluid dynamic processes and offer a unique means of isolating thermochemical non-equilibrium from broader flow complexities. As such, they provide a controlled environment to examine core thermochemical processes under flight-relevant enthalpy conditions.

Both gas radiation and thermochemistry can be effectively studied using optical diagnostics methods such as optical emission spectroscopy (OES) and laser absorption spectroscopy (LAS). The use of LAS has grown in recent years, driven by advances in high-speed tunable diode lasers and quantum cascade lasers [9, 10]. LAS probes the lower states of radiative transitions, enabling absolute number density measurements of low-energy quantum levels.

Scanning absorption spectroscopy techniques employ a spectrally narrow light source whose central wavelength is rapidly tuned across the absorption feature. By sweeping over the absorption line to detect the transmitted intensity, the line shape and absolute absorbance can be extracted, from which translational temperature and lower state number density may be inferred. Broadband light sources can also be used, but require a high-resolution spectrometer to resolve

---

*DPhil Student, University of Oxford, Oxford Thermofluids Institute, United Kingdom.
†Associate Professor, University of Oxford, United Kingdom.
‡Professor, University of Oxford, Atomic and Laser Physics, United Kingdom.
§Professor, University of Oxford, Oxford Thermofluids Institute, United Kingdom
¶DPhil Student, University of Oxford, Oxford Thermofluids Institute, United Kingdom
‖Associate Professor, University of Oxford, Oxford Thermofluids Institute, United Kingdom
**Associate Professor, University of Oxford, Oxford Thermofluids Institute, United Kingdom

absorption features. In the present study, a broadband light source is chosen, as it provides an instantaneous snapshot of the shock wave without requiring active tuning during the brief microsecond-scale experiment. As part of this work, a bespoke modeless laser was developed to probe nitric oxide (NO) absorption features near 226 nm. The modeless design permits flexible control over the spectral output, allowing fine tuning of the central wavelength(s) and bandwidth.

II. Experimental Arrangement

These experiments are complementary to VUV and UV emission spectroscopy experiments performed in the Hypersonics Group at the University of Oxford at the same test conditions, earlier during the same test campaign. Further publications will show the complementarity of the two diagnostics methods to characterise gas thermochemistry [11].

A. T6 Stalker Shock Tube

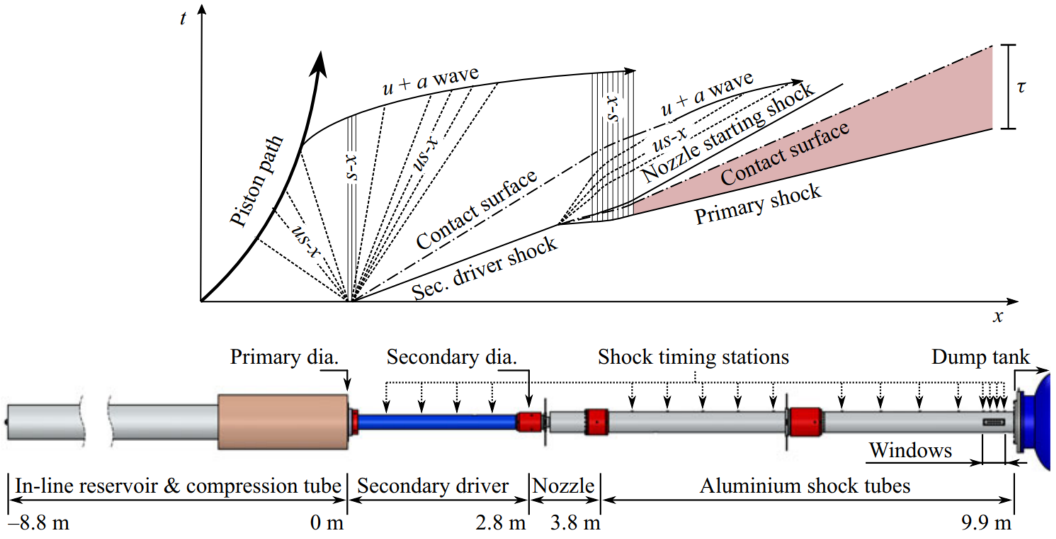

Fig. 1 Schematic overview of the T6 Stalker Tunnel T6 in Aluminium Shock Tube mode [8].

The T6 Stalker Tunnel [12–15] was used in shock tube mode (Figure 1) to reach high shock velocities. The facility's large tube diameter provides a long optical path, allowing high signal-to-noise ratio in the measurement of spectroscopic data. For emission spectroscopy, exposure times can be minimised, consequently reducing spatial blurring effects due to shock motion during acquisition, which is a major contributor to the instrument spatial resolution function. For absorption spectroscopy, weaker absorption features can be resolved as absorbance is linearly proportional to the path length according to Beer-Lambert law.

The shock wave created by the bursting of the primary diaphragm passes through a secondary driver, is expanded through a nozzle to a larger tube diameter, and subsequently passes by a set of opposing optical windows. The imaging optics employed in this work view the flow through these windows. 17 flush-mounted piezoelectric pressure sensors along the length of the facility ("shock timing stations" in Figure 1) record the arrival time of the shock wave, which allows subsequent rebuilding of the shock speed and history. The pressure readings are also used to trigger the intensified camera and laser pulse to respectively image and interact with the shocked gas as it passes the windows' location. The propagation path of the laser sheet through the tunnel test section is discussed in Section II.B, and coupling of the imaging optics to T6 in Section II.C.

B. Modeless Laser

Transitions of interest are centered around the 226 nm region, probing ground-state NO to measure number densities. A modeless dye laser was selected for these experiments, offering a tunable, spectrally smooth broadband source with variable bandwidth to target several lines simultaneously. By operating without a resonant cavity, the modeless laser [16] produces a continuous spectrum, in contrast to the discrete longitudinal modes characteristic of conventional

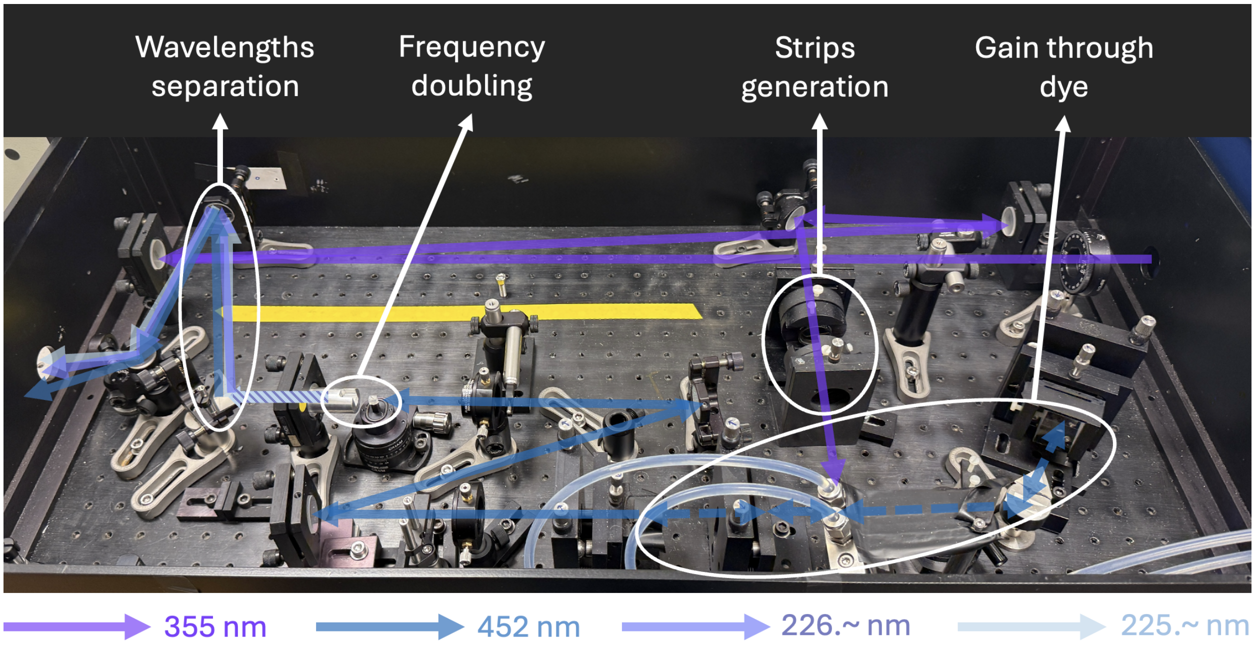

Fig. 2 Modeless laser internal optical path and components.

laser systems. This spectrally continuous output is particularly well-suited for recording molecular absorption spectra comprising narrow features, which may otherwise fall between the modes of standard broadband lasers and go undetected.

Moreover, the modeless configuration significantly suppresses so-called "mode noise", both in amplitude and frequency, that often complicates the interpretation of relative intensities in recorded spectra [17–19]. In all other respects, the output of the modeless laser retains the attributes of conventional systems: a high degree of collimation suitable for extended beam paths, precise steerability through the interrogation region, and efficient coupling into the spectrometer for accurate spectral acquisition. The modeless laser optical layout is shown in Figure 2, and the working principles of its different components detailed in this section.

A system comprising two prisms and a strip mirror replaces the resonant cavity of a conventional laser, as illustrated in Figure 3. When the dye solution flowing in the cell positioned between the prisms is excited by an external pump source, it emits spontaneously at a wavelength characteristic of the dye composition and pump wavelength combination. In this set-up, excitation is provided by a flashlamp-pumped nanosecond Surelite I-10 Nd:YAG laser operating at its third harmonic (355 nm). The fundamental and second harmonics (1064 nm and 532 nm) are dumped into a separate enclosure outside the laser head, while the 355 nm beam is directed through a lens system to expand the beam before it passes through a four-faceted prism and a cylindrical lens, as shown in Figure 4a, generating four parallel excitation stripes within the dye cell. The 0.28 $g.L^{-1}$ solution of Coumarin II in ethanol emits a broadband spectrum centred around 452 nm.

Spontaneous emission from the stripe aligned with the strip mirror is retro-reflected onto the dye cell to the tuning prism (Figure 4b). The beam is turned by the tuning prism to travel back through the cell, parallel to the incident beam, offset to pass through the next adjacent pumped stripe where it undergoes further amplification. The pair of TIR prisms, with slightly offset apexes, generates a travelling wave that sequentially passes through all four excited regions in the dye, gaining energy at each pass without the formation of a resonant cavity, as shown schematically in Figure 4b. The dye cell itself is angled to prevent cavity formation, which would otherwise lead to the development of longitudinal modes.

The travelling wave is spectrally dispersed by a pair of dispersing prisms located between the cell and the first tuning prism (Figure 4b). Adjusting the incidence angle at the tuning prism allows the output wavelength to be further selected. This spectral narrowing concentrates the emission into a smaller bandwidth than the natural dye fluorescence range, thereby enhancing spectral brightness and improving conversion efficiency in the downstream phase-matched frequency doubling crystal. The top edge of the second tuning prism, referred to as the cut-off prism, is trimmed to allow the beam to exit the amplification path shown schematically in Figure 4b.

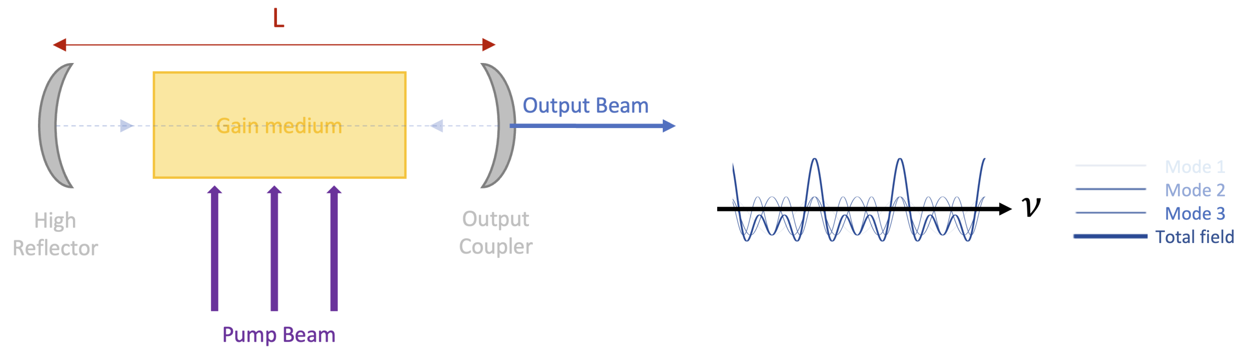

(a) Traditional laser schematic **(b) Traditional laser multimodal output**

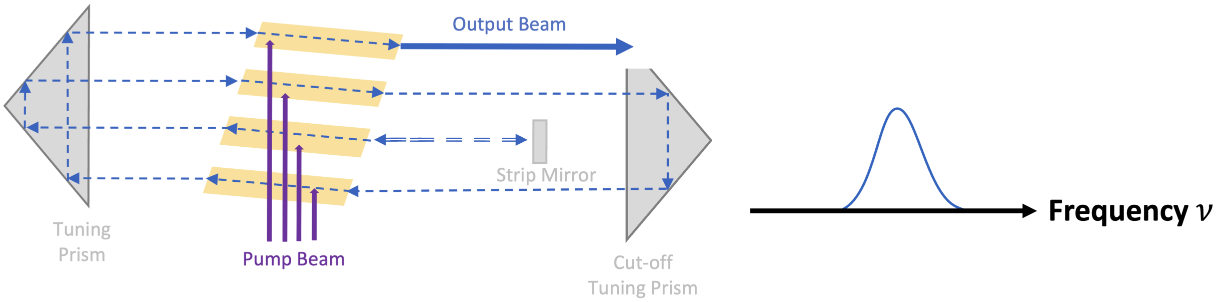

(c) Modeless laser schematic **(d) Modeless laser continuous spectrum**

Fig. 3 Comparative schematic of a traditional laser and modeless laser gain media. In a traditional laser, several longitudinal modes determined by the cavity length L, with frequency spacing given by $\Delta\nu = \frac{c}{2nL}$ are present. In contrast, the modeless laser exhibits a continuous spectrum without discrete longitudinal mode fluctuations.

The 452 nm output beam is subsequently frequency-doubled to 226 nm using a critically phase-matched beta barium borate (BBO) crystal. Owing to the crystal's nonlinearity, the fundamental 452 nm wave induces a nonlinear polarisation response that oscillates at twice the input frequency, producing the ultraviolet output. The resulting 226 nm beam is then separated from the residual 452 nm fundamental using a Pellin–Broca prism, as illustrated in Figure 5a.

The spectral width of the second harmonic at 226 nm was initially found to be narrower than required for this application. Ideally, the final beam should exceed the spectral resolution of the receiving optics, broad enough to resolve multiple absorption lines simultaneously. Two strategies were pursued: first, a cylindrical lens was positioned ahead of the BBO crystal to expand the 452 nm beam in the critical plane, causing it to focus within the crystal over a wider range of angles. Since the refractive index of the crystal is wavelength-dependent, efficient harmonic generation across a broader spectral range requires different phase-matching angles for different wavelengths. This method did result in a broadened spectral profile, but a second approach proved more versatile: introducing a second BBO crystal in series with the first. This set-up enabled the generation of two distinct output beams from the 452 nm fundamental, as illustrated in Figure 5b. The remaining 452 nm light exiting the first crystal undergoes frequency doubling in the second, producing a second output around 226 nm. By fine-tuning the orientation of each crystal, both ultraviolet outputs can be independently adjusted in wavelength. This configuration allows for two spectrally broadened beams with wavelength separation up to 3 nm within the 224–227 nm range, or alternatively, the two beams can be combined to form a single spectrally broader output at any chosen wavelength within that span, as shown in Figure 5c. The relative intensity of the two beams may be controlled by adjusting the central wavelength of the modeless laser output. By angle-tuning the dispersing prisms and selecting the appropriate region of the dye laser spectrum, the intensity balance between the two beams can be optimised.

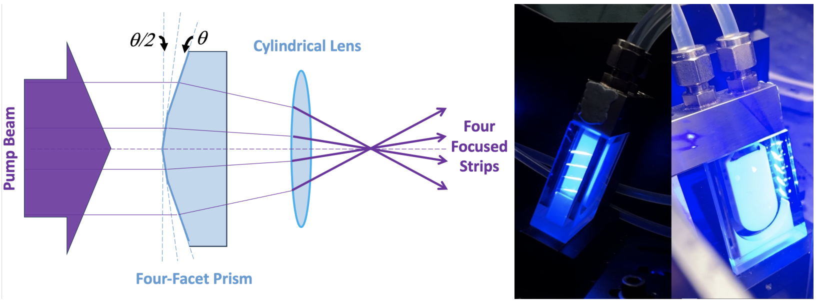

(a) Schematic of stripes generation using a four-facet prism and a cylindrical lens (left). Pictures of the four discrete strips on the dye cell (right).

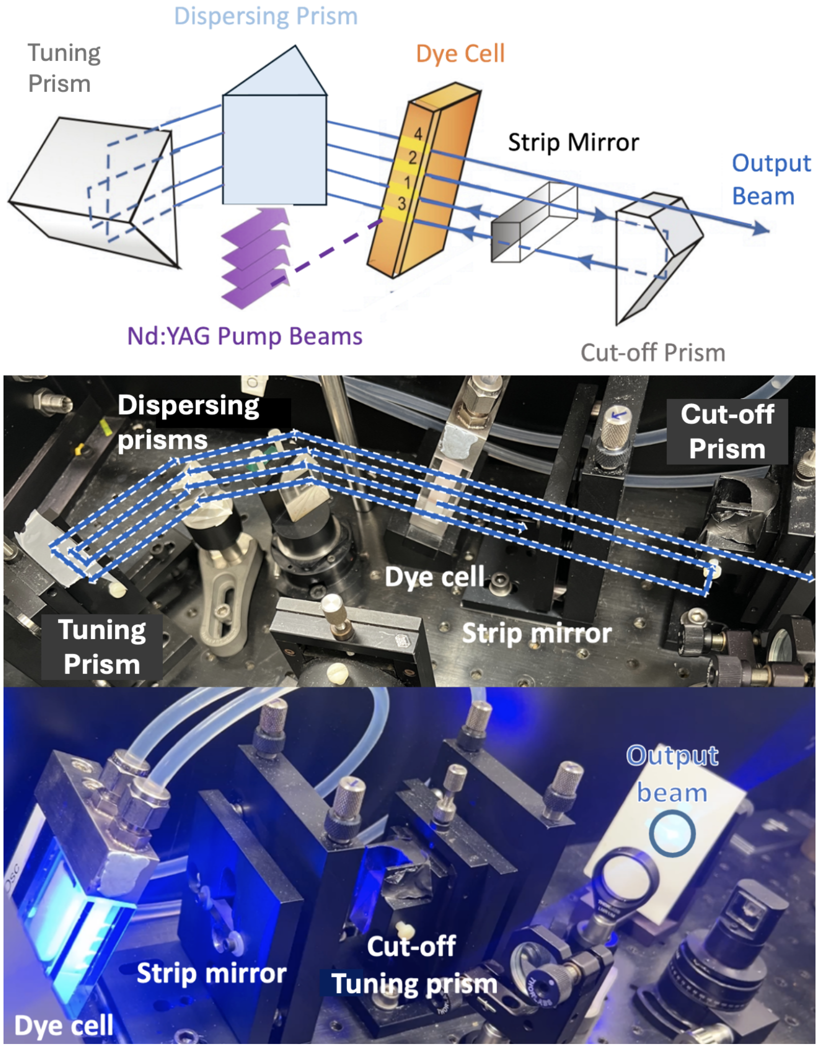

(b) Internal setup of the modeless generation - schematic (top) compared to physical elements (middle and bottom). The dye cell emits a broadband spectrum centred at 452 nm when pumped by a third harmonic Nd:YAG laser at 355 nm.

Fig. 4 452 nm generation and amplification from the 355 nm Nd:YAG laser.

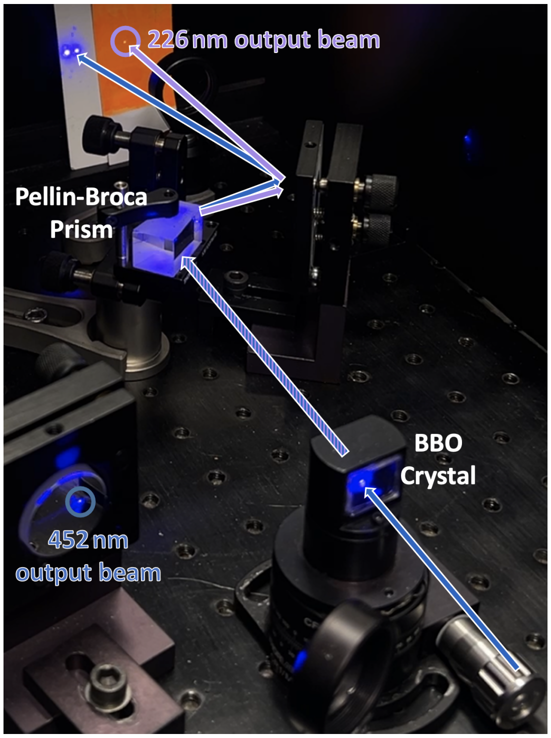

(a) Internal set-up of the second harmonic generation: a single BBO crystal frequency-doubles the 452 nm beam and the Pellin-Broca prism separates it from the remaining 452 light. The 226 nm beam is rendered visible by fluorescence on the orange card at the top right of the photograph.

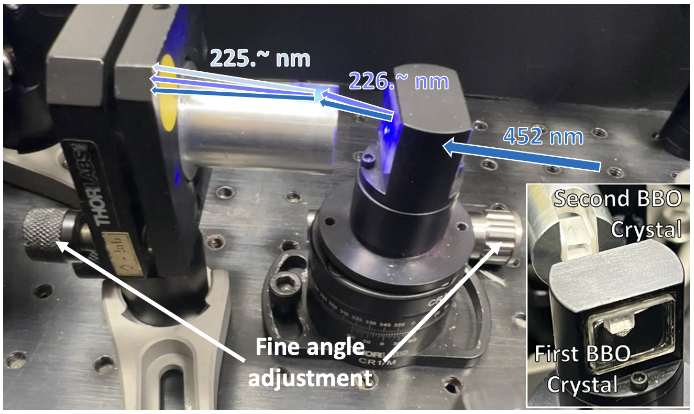

(b) BBO crystals in series to generate two beams of variable wavelengths from the 452 nm fundamental beam.

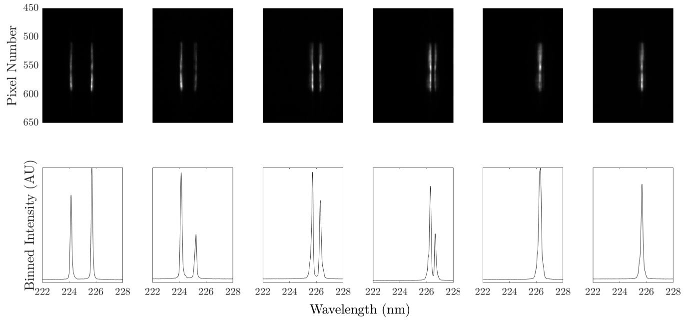

(c) Wavelength and relative intensity tuning by adjusting the BBO crystals angles.

Fig. 5 Second harmonic generation using BBO crystals

The laser system is located in a dedicated laser room adjoining the tunnel room. An aperture in the shared wall houses a dual-shutter mechanism, with each shutter connected to the interlock system of its respective room. The laser beam travels through the tunnel room, passing a few centimetres above ground level beneath T6, and continues to the test section where a periscope arrangement brings it up to the tunnel centreline, as shown in Figure 6. Along its path, the beam is fully enclosed within anodised aluminium channels and chambers surrounding turning mirrors. These mirrors are optimised for 45° incidence, with p-polarisation reflectivity coefficients less than 2% below those for s-polarisation, minimising intensity losses at the periscopes.

To obtain spatially resolved absorption spectra, the laser must illuminate the full extent of the field of view under investigation, ensuring simultaneous interaction across all spatial points. This requires expansion of the beam into a laser sheet. The optical configuration used for this purpose is shown on the right side of Figure 6: a cylindrical concave lens with focal length $f = -25$ mm, followed by a spherical convex lens with $f = 200.7$ mm, spaced by the sum of their focal lengths, expand and collimate the beam within the test section.

The laser enters the test section through a magnesium fluoride (MgF_2) optical window and exits through the diametrically opposite window on the receiving optics side after probing the gas slug behind the shock front. The partially absorbed laser light is then redirected by the mirror system described in Section II.C onto the spectrometer, where it is imaged by an intensified camera to produce a spatially resolved absorption spectrum.

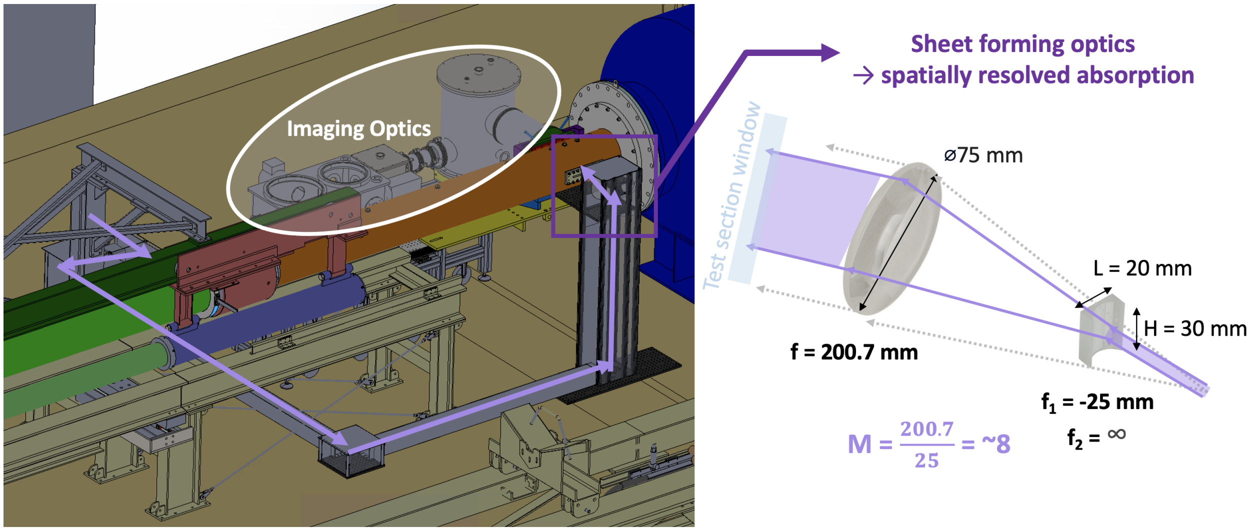

Fig. 6 Schematic of the laser path (lilac arrows) from the laser room to the tunnel test section (left). Series of optics turning the laser beam into a laser sheet (right).

C. Imaging Optics

The recently developed vacuum-ultraviolet (VUV) emission spectroscopic system [20, 21] is used to image the laser sheet as it exits the test section. Even though longer wavelengths in the ultraviolet, visible and near infrared are accessible, the system is optimised towards wavelengths between 116 nm and 250 nm where the quantum efficiency of the camera detector and blazing angle of the dispersion grating are greatest. The system consists of five VUV-enhanced aluminium and magnesium fluoride (MgF_2) coated mirrors redirecting the signal from the test section centerline to a VUV Spectrometer (McPherson 207V). A 1200 $gr.mm^{-1}$ grating is mounted in the spectrometer for fine spectral resolution (Section III.B.2). An intensified P43 iStar sCMOS camera is connected to the spectrometer to record the spectra and generate a spatially resolved image. The mirrors are used in a telecentric configuration shown in Figure 7a, to reduce spatial blur and obtain the highest fidelity and intensity of signal [20, 22] . All optics have the same f-number ($f/\# = 4.7$) as the spectrometer to avoid under-filling or stray light interferences, setting the magnification of the system as the ratio of the two powered mirrors' focal lengths $M_{\mathrm{system}} = \frac{f_{\mathrm{collimating}}}{f_{\mathrm{focusing}}} = 7.84$. A cylindrical mirror is used to correct the system's astigmatism caused by the finite angle of incidence to the powered mirrors [20, 22]. Mirrors dimensions and locations were chosen using an optimisation code which took as inputs geometrical and optical constraints, and output mirrors' parameters to optimise field of view, leading to 94 mm imaged along the test section centerline. The optical configuration is shown in ray-tracing in Figure 7b, and further details on the receiving optics design can be found in literature [11, 20, 21].

III. System Optical Performance and Characterisation

Precise understanding of the optical system's capability and resolution is essential to assess the trustworthiness and limitations of the data acquired, as well as to adopt the most appropriate approach during analysis.

A. Modeless Laser Characterisation

To analyse absorption data, accurate characterisation of the laser beam interacting with the gas is critical. The beam was characterised in terms of its intensity and wavelength stability for different operating conditions.

1. Intensity Variation

With Gating

The 10 Hz repetition rate of the Surelite pump laser, corresponding to one laser pulse every 100 ms, presented challenges for synchronisation with the arrival of the shock wave in the test section. Operating the laser outside its nominal 10 Hz repetition rate leads to variations in pulse characteristics, as measured by a photodiode and illustrated in

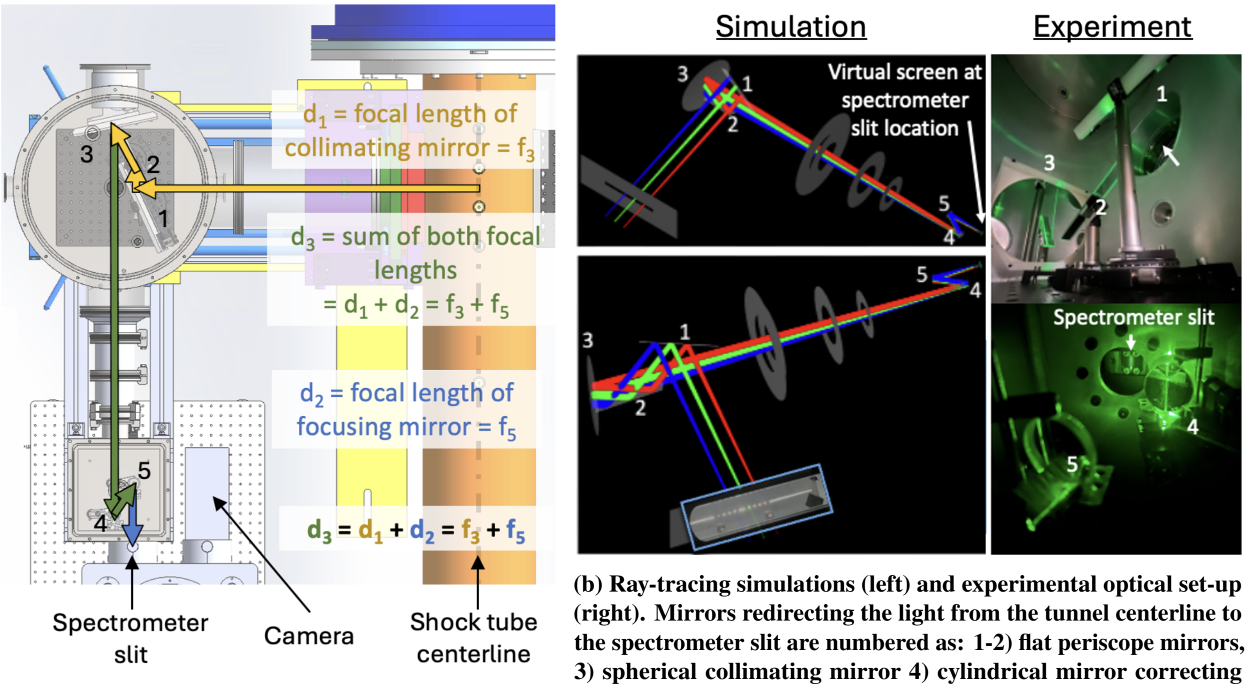

(a) Geometrical equalities required for telecentricity.

(b) Ray-tracing simulations (left) and experimental optical set-up (right). Mirrors redirecting the light from the tunnel centerline to the spectrometer slit are numbered as: 1-2) flat periscope mirrors, 3) spherical collimating mirror 4) cylindrical mirror correcting astigmatism 5) spherical focusing mirrors.

Fig. 7 Receiving Optics Configuration

Figure 8. Attempting to generate an additional single pulse while running the laser continuously introduces a high risk of misfiring, particularly if the triggered pulse occurs too soon after the previous one: anything below a 50 ms interval resulted in a failure to fire. The alternative approach of inhibiting ('gating') the laser for a duration significantly longer than its 100 ms cycle produced shorter, more intense pulses, which posed a risk of damaging the laser itself, the dye cell or downstream optics. Nonetheless, this method was considered preferable to the risk of misfiring and missing a T6 shot, and gating the pump laser for shot-specific durations was adopted as the operational approach. The behaviour of the modeless laser under different gating conditions, highly sensitive to dye excitation conditions, gain efficiency, and the frequency doubling process, was assessed independently.

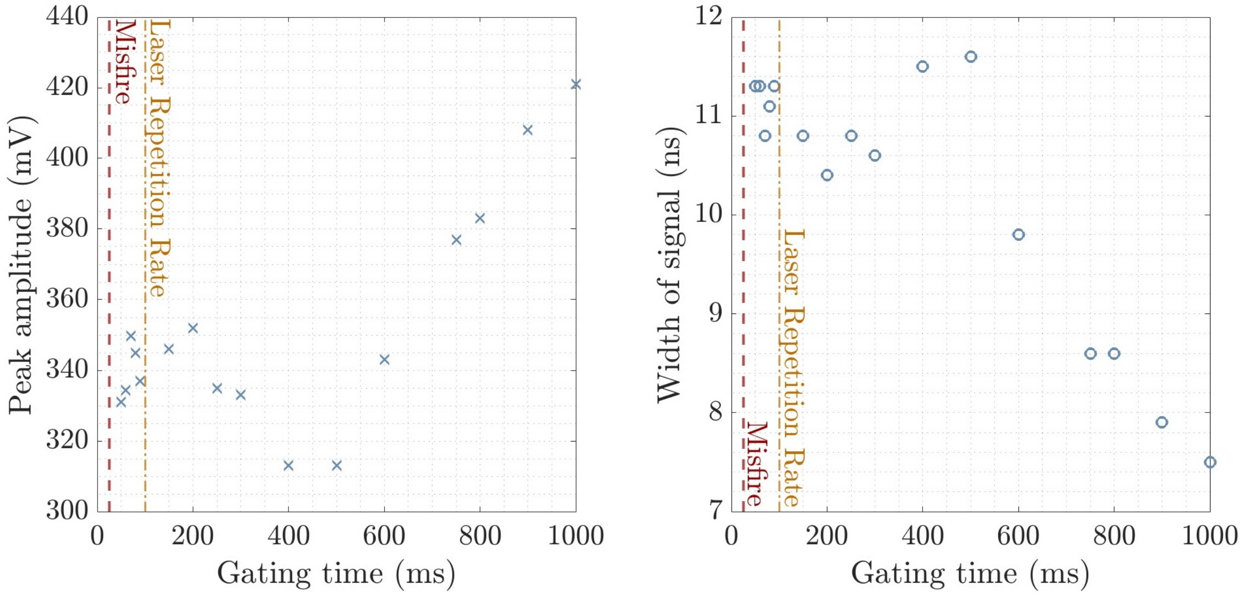

Fig. 8 Surelite I-10 Nd:YAG pulse behaviour when operated outside of its design 10 Hz frequency. 'Amplitude' and 'width' refer to the properties of the laser light pulse as measured by a biased photodiode.

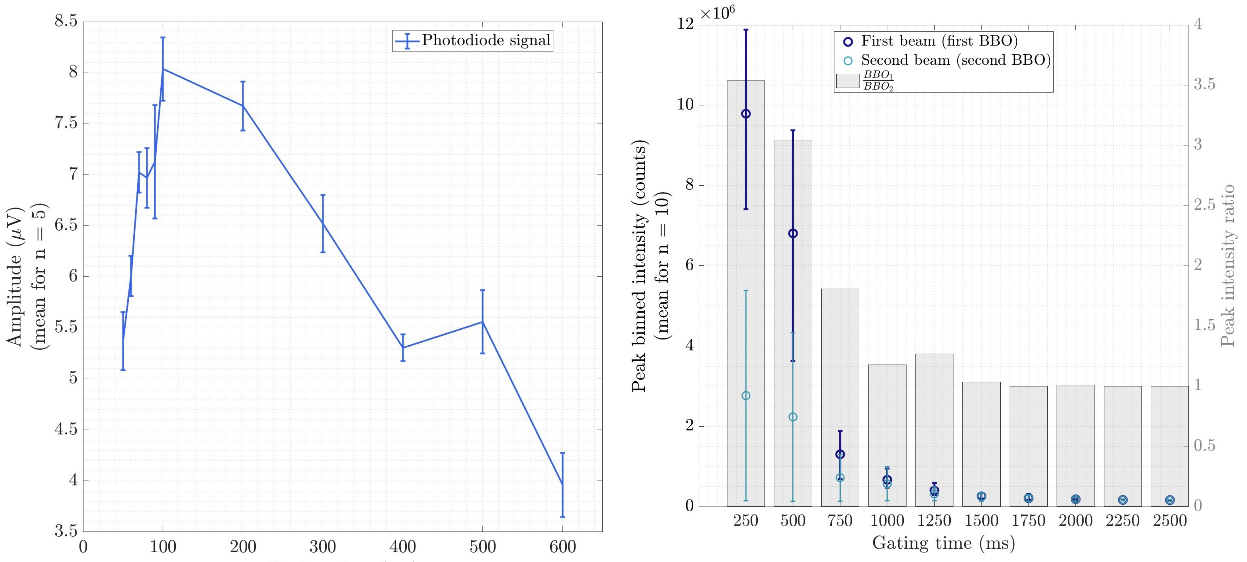

(a) Intensity recorded by a photodiode placed at the exit of the modeless laser, averaged over 5 measurements. Error bars indicate the variation across the five repeated measurements.

(b) Signal resolved by the CCD camera to differentiate the two frequency doubled beams intensity variations, averaged over 10 measurements. The grey bars show how their peak intensity ratio varies (right axis) with gating times.

Fig. 9 226 nm modeless laser intensity variation with gating times

The 226 nm modeless laser's intensity behaviour followed the opposite trend to the Surelite's shown in Figure 8. When gated, the pulse intensity of the beams decreases severely, as shown in Figure 9a. This observation is thought to be caused by the crystal cooling. In steady state operation, some laser energy is absorbed by the BBO, raising its temperature. This is the condition at which phase matching angle was optimised. When the laser is gated, the crystal cools which varies the material refractive index, affecting phase matching and causing reduced conversion efficiency. This effect was particularly strong for the first crystal, which was cooling faster due to its smaller size and lack of isolation. This difference leads to a change in relative intensity between the two beams with gate time. This can be seen in Figure 9b: the beam generated by the first crystal is over 3.5 times stronger than the one generated by frequency doubling through the second crystal for a gating time of 250 ms, but the ratio rapidly asymptotes to 1 as gating time increases. To keep the ratio stable over a range of gating times, thermal housings will be used in future work to maintain the crystals at constant temperature when they are not heated up by the fundamental pulses.

For gating durations shorter than the laser's nominal 100 ms repetition rate, the photodiode signal also drops sharply, as shown in Figure 9a. As shown in Figure 8, the Surelite pump beam becomes both more intense and shorter in duration at reduced gating times. This could raise the crystal temperature above the phase-matching condition established during alignment at 10 Hz, thereby reducing frequency doubling efficiency. Additionally, the altered pump characteristics may affect the excitation dynamics of the dye, influencing the 452 nm modeless output.

In Space

Characterising the spatial intensity profile of the laser is critical for accurately retrieving absorption features across the measurement domain. If the laser intensity varies spatially, the same absorption line can appear with different intensities at different locations. It is therefore essential to understand the spatial distribution of the laser intensity interacting with the gas along the field of view.

This characterisation is carried out for ten gating durations ranging from 250 ms to 2500 ms, previously shown to affect the overall beam intensity. Representative profiles for 250 ms and 1000 ms are shown in Figure 10.

The intensity profile exhibits visible spatial variation, with generally higher signals in the upper half of the sensor. This may result from non-uniformities in the beam sheet or spatial sensitivity differences in the camera intensifier. Despite these variations, the overall profile shape remains consistent across gating durations, with recurring local peaks and dips at the same spatial locations. The magnitude of variation around the mean decreases with longer gating durations, as summarised in Table 1. All but one gating duration used in the experiments lie between 900 ms and 1500 ms, where spatial variation is relatively low. However, increasing the gating duration also reduces the signal-to-noise ratio, as seen in the higher background noise and the elevated baseline of Figure 10b relative to Figure 10a.

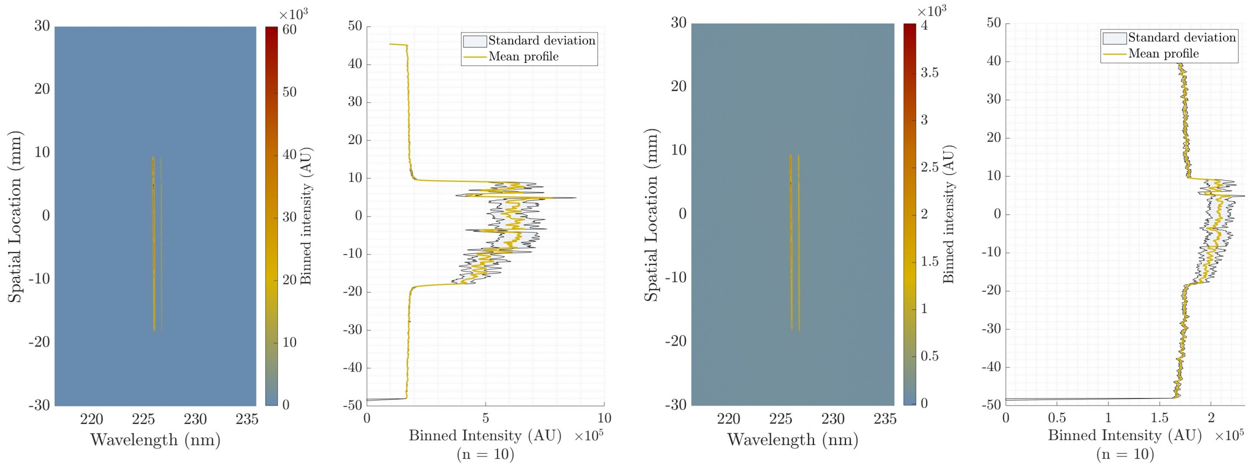

(a) 250 ms gating duration

(b) 1000 ms gating duration

Fig. 10 Spatial intensity profile variation of the 226 nm modeless laser for two gating times. The left images display the spectro-spatial average over 10 acquisitions, while the right images present the wavelength-binned profiles along with the bounds derived from the 10-image dataset.

Gating duration (ms)	250	500	750	1000	1250	1500	1750	2000	2250	2500
Max. upper deviation (%)	32.4	37.2	19.4	16.6	10.6	8.0	7.0	6.5	3.5	4.0
Max. lower deviation (%)	21.7	33.8	18.4	10.2	6.0	4.6	3.3	3.3	2.8	3.6

Table 1 Intensity maximum local deviation from mean over 10 acquisitions for various gating durations. Profiles for 250 ms and 1000 ms cases can be seen in Figure 10.

2. Wavelength Variation

Just as with beam intensity variation, wavelength variability had to be quantified to ensure that the correct spectral locations were probed for the relevant experiment.

With Gating

The output wavelength of a BBO crystal in a frequency-doubling set-up is sensitive to its temperature because the refractive indices of the crystal vary with temperature. This dependence directly affects the phase-matching condition, which determines the fundamental wavelength most efficiently converted to its second harmonic. In this experiment, the crystals were aligned for phase matching at the nominal 10 Hz repetition rate, when continuous pumping maintained them at a stable operating temperature. Cooling of the crystal, such as that caused by reduced intrinsic heating during extended gating periods, shifts the phase-matching wavelength and can move the output away from the intended spectral location. Consequently, gating-induced temperature changes could affect both the conversion efficiency and the precise output wavelength. The data collected during the spatial variation study was used to quantify the shift in the two peak wavelengths for a range of gating times, and is shown in Figure 11 for gating times of 250 ms and 1000 ms. The maximum deviations from the averages are presented in Tables 2 and 3 for the first and second beams respectively. The largest observed wavelength shift from the average is only 0.4%, with most gating durations showing no measurable effect on the central wavelength.

Gating duration (ms)	250	500	750	1000	1250	1500	1750	2000	2250	2500
Max. +ve λ shift (%)	0.0067	0	0	0	0.0067	0.33	0	0.0135	0	0.4028
Max. -ve λ shift (%)	0	0.0067	0	0	0	0.0135	0.0201	0	0.3289	0

Table 2 Maximum wavelength shift for the first BBO crystal versus mean over 10 acquisitions for various gating durations. Profiles for 250 ms and 1000 ms cases can be seen in Figure 11.

Gating duration (ms)	250	500	750	1000	1250	1500	1750	2000	2250	2500
Max. +ve λ shift (%)	0.007	0	0.007	0	0.007	0	0	0.007	0	0.007
Max. -ve λ shift (%)	0	0	0	0	0	0	0.0211	0.007	0.007	0

Table 3 Maximum wavelength shift for the second BBO crystal versus mean over 10 acquisitions for various gating durations. Profiles for 250 ms and 1000 ms cases can be seen in Figure 11.

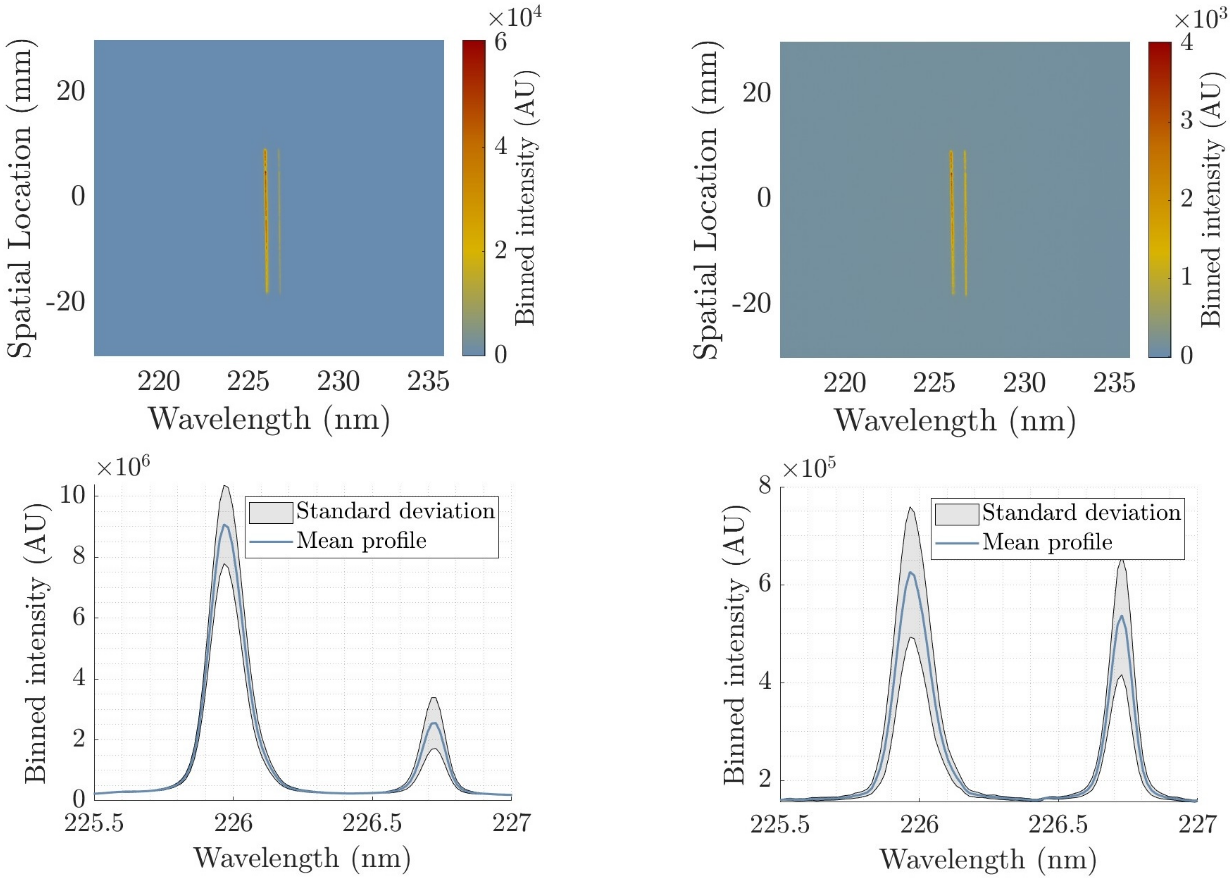

(a) 250 ms gating duration

(b) 1000 ms gating duration

Fig. 11 Spectral profile variation of the 226 nm modeless laser for two gating times. The top images display the spectro-spectral average over 10 acquisitions, while the lower images present the spatially-binned profiles along with the bounds derived from the 10-image dataset.

In Space

Because the refractive index of a BBO crystal is wavelength-dependent, the second harmonic waves generated by the two crystals would emerge at slightly different angles, with their divergence further increased by the Pellin–Broca prism. It was therefore necessary to characterise the spatial variation of wavelength in the beam to ensure that all regions of the test section were probed with the same input wavelength. Inspection of the beam profile on the camera sensor confirmed that there was no wavelength variation along the sensor's spatial axis, indicating homogeneity in that plane. This behaviour was expected, as the final periscope raising the beam to the test section height also rotates the beam such that any wavelength variation lies across the beam's thickness rather than its height, as illustrated in Figure 12.

Wavelength variation across the beam's thickness was also examined. With the beam expanded to fill the test section window, portions of its height (corresponding to different horizontal planes in the test section) were blocked to check for wavelength shifts. No change was observed on the camera's sensor. The beam was then scanned through the spectrometer slit by rotating the focusing mirror (mirror N°5 in Figure 7). Small changes in beam position, of the order of a few pixels, suggested that the wavelength did vary slightly across the beam thickness, and that the laser sheet contained a broader spectral range than that used during experiments.

This effect was more apparent when observing the divergence directly at the output of the modeless laser box, implying that the eight turning mirrors used to relay the beam to the test section provided some spatial mixing. At the output of the BBO crystal, the wavelength variation was measured to be less than 1 nm over a 5 mm traverse scan. In future work, spatial variation of spectral content will be reduced by introducing a pair of prisms before the lens focusing the beam onto the crystal, in order to separate the light into parallel wavelength components. A matching prism system after the crystals will be used to recombine the wavelength components into a spatially homogeneous beam.

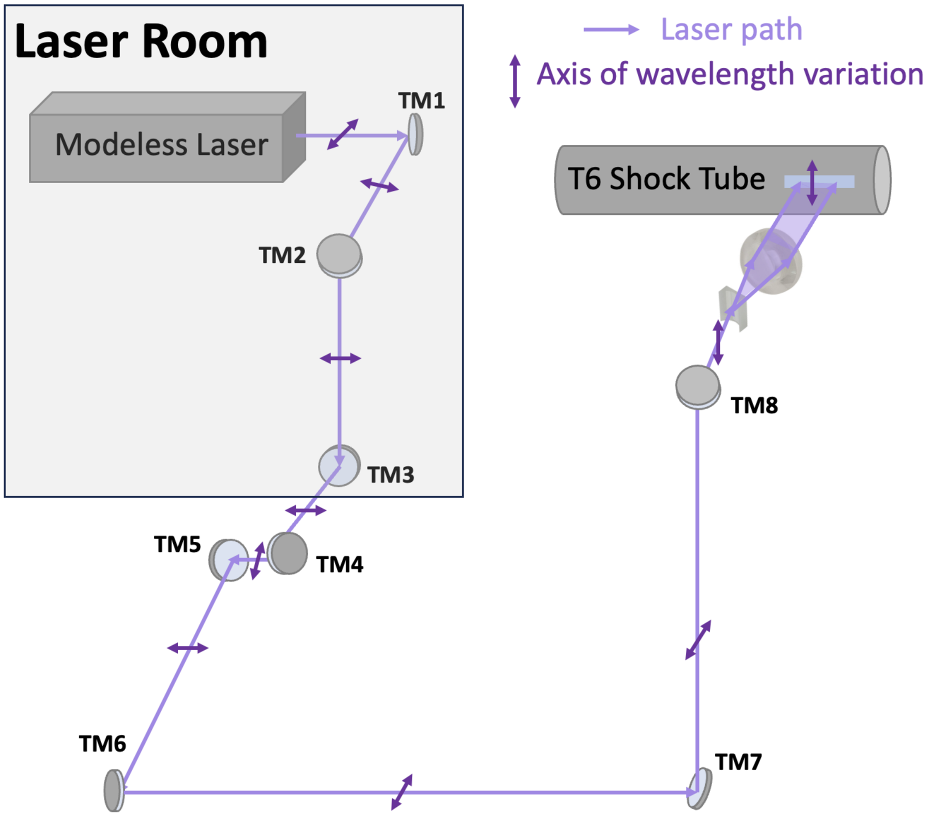

Fig. 12 Schematic of the turning mirrors (TM) used to relay the output of the modeless laser to the test section. TM1 to TM3 are located in the laser room, TM4 to TM8 in the tunnel room. TM2-TM3 and TM7-TM8 are periscope systems which change the horizontal plane of the laser from the height of the modeless laser to ground level, and from ground level to the height of the test section respectively.

B. Imaging Optics Performance

The imaging optics were characterised as part of the optical emission spectroscopy test campaign, and further details can be found in literature [11].

1. Spatial Calibration and Resolution

Calibration

Spatial calibration is performed using a calibration plate with distinctive apertures (visible in transparency at the bottom left of Figure 7b), flushed against the test-section window as shown in Figure 13a. The “cut-out” laser beam signal travels through the apertures and is imaged onto the camera’s sensor, such that the region of the test section under observation can be identified, as shown in Figure 13b.

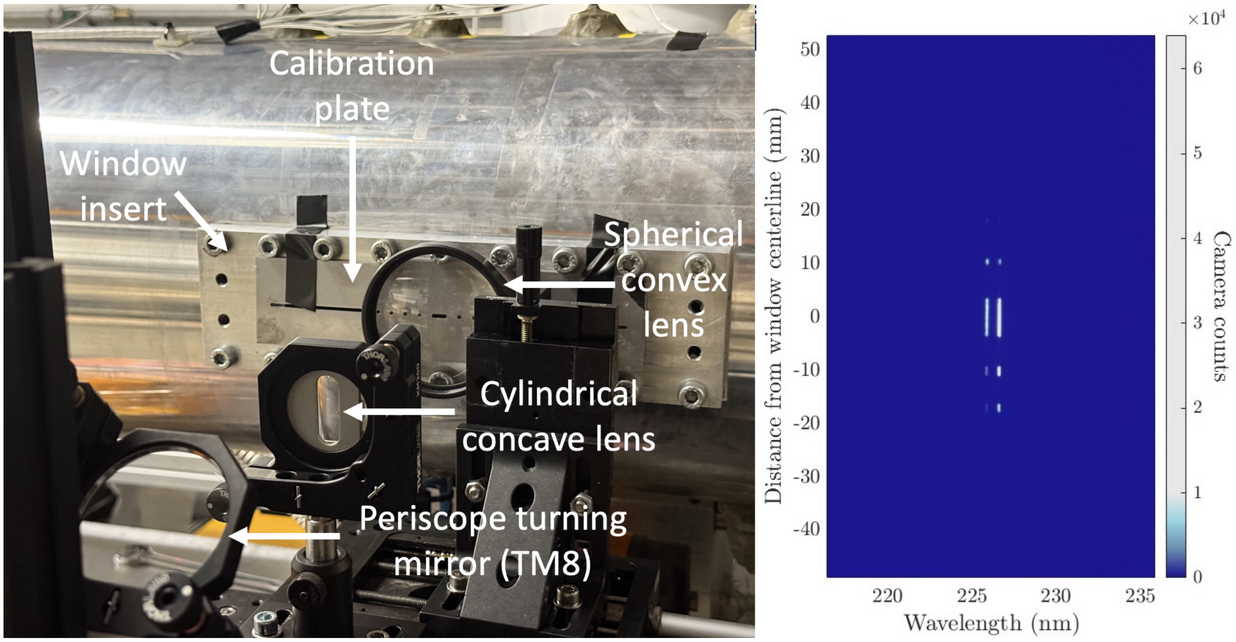

(a) Calibration plate located at the window **(b) Laser through calibration plate**

Fig. 13 Laser beam spatial calibration

Spatial Resolution Function (SRF)

The Spatial Resolution Function (SRF) describes the capacity of the optical system to resolve and distinguish spatial features. The closer the SRF is to a Dirac delta function, the better the system is at differentiating two adjacent events. The FWHM of the SRF serves as a quantifier of the blurring effect on the physical phenomena imaged during acquisition.

The methodology followed to spatially calibrate and characterise the optical system broadly follows the approach adopted in the NASA Ames EAST facility [23], and divides the SRF in three components: 1) the Line Spread Function (LSF) or resolution of the collection optics and camera CCD sensor, 2) the Optical Resolution Function (ORF) which captures the geometrical averaging of off-axis radiance emitted over the width of the tunnel's cross section and collected by the aperture, and 3) the shock motion during gating time. Further effort was put into obtaining asymmetric, spatially-varying LSF fit to various models, more representative of the two-dimensional sensor surface and imperfect experimental set-up. Details can be found in related publications [11].

To model the LSF, a white light back-lit knife edge was placed at the tangential focus, i.e at the centreline of the tube, where the optical system was focused. This sharp edge was imaged at 12 discrete locations along the field of view to cover the entire sensor length, of which two examples are shown at the top of Figure 14. These images were rotated by 0.33° to correct for camera angle. This correction is essential to avoid artificially worsening the LSF, as binning an angled line would spread the energy emitted from the tangential focal plane over multiple pixel rows, just like a spatial blur.

After rotation and binning over all wavelengths, the signal at the knife-edge location was plotted to obtain the Edge Spread Function (ESF), shown on the third row of Figure 14. The ESF is centered on the location of the steepest gradient of the function, and delimited on each side by a baseline level where the gradient relaxes to less than $\frac{1}{100}$ of its maximum, and the closest local maximum of the function (second row of Figure 14). The minimum of the function is subtracted as the off-set, and the function normalised. The experimentally measured LSF is approximated by the derivative of the ESF.

Four models were subsequently fitted to each local experimental LSF: 1) a pure Gaussian, 2) a pure Lorentzian, 3) a Voigt, and 4) a hybrid weighted Voigt, to characterise the spatially varying behaviour of the sensor and of the optics. Indeed, the LSF showed varying degrees of asymmetry due to sensor non-uniformity or optical aberrations. The LSF zero-location was taken to be its center of mass instead of its maximum, to reflect the mean position about which energy was spread and to allow a fairer comparison between models.

Examples of models fitted at different locations can be seen in row 4 of Figure 14. Note the apparent variation in

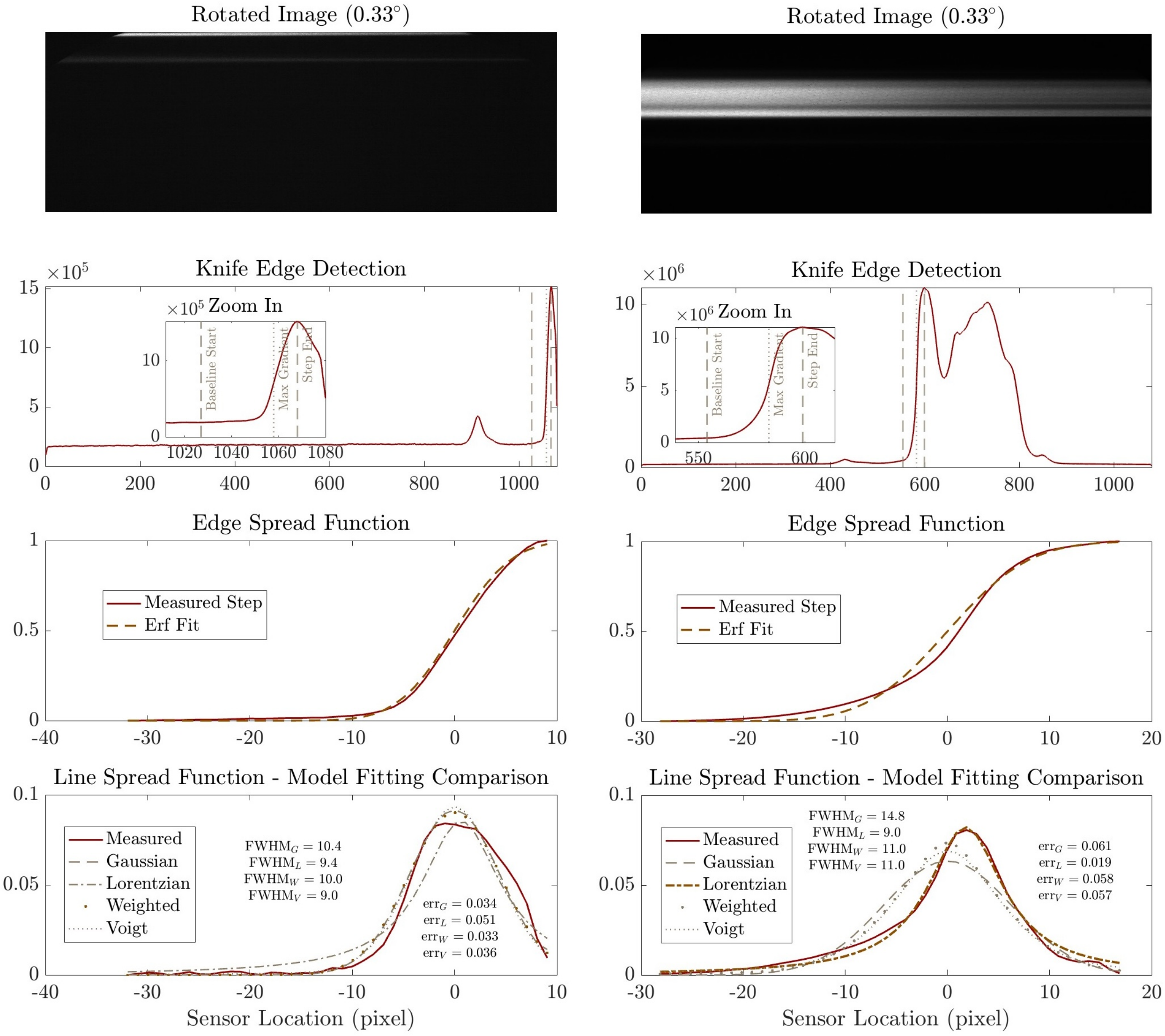

(a) Example fitting for the most downstream location.

(b) Example fitting for the middle section location.

Fig. 14 LSF fitting from knife-edge images. First row: rotated image, second row: knife-edge detection, third row: Edge Spread Function (ESF), last row: fitting of data to the four different models.

asymmetry and tail size with location. To assess which model performs better in reproducing the measured LSF, the Euclidean norm of the residuals was computed for each case. The total deviation between the models and the data across all points is shown in the legend of Figure 14, and the best fit emphasized in dark orange. For each location, the model yielding the lowest residual norm was considered the best representation of the measured local LSF, and kept to reconstruct the sensor LSF surface.

Each individual LSF was originally discretised over a shorter local spatial axis centred around its center of mass. To integrate the family of LSFs onto a consistent framework for interpolation and convolution, each LSF was zero-padded to a retrieve full-length array representative of the physical sensor size of 1080 pixels. The LSF support axis was however selected to be 1081 pixels to enforce an exact center, which was necessary for later convolution with symmetric functions defined over the same kernel support axis. The resolution difference of one pixel was judged to have a negligible impact on modelling. Figure 15a (a) shows the resulting model LSFs aligned to their relevant positions along the camera sensor. Linear interpolation between these individual functions was used in order to generate a suitable LSF for every camera row, as seen in Figure 15a (b). It has been assumed that the LSF varies smoothly along the camera sensor. Figure 15a (c) shows a 'top down' view of the interpolated LSF behaviour, from which the parts of the sensor more prone to asymmetry can be more easily observed.

The experimentally measured, spatially varying LSF was then convolved with the ORF and Shock Motion kernels as explained in [23] to construct the SRF at each sensor location.

Figure 15b illustrates how the ORF, or collection cone, evolves along the optical path. Using the Gaussian optics model implemented in Optometrika [24], the signal received from a 1 mm diameter bundle of rays at the test section centreline is simulated and plotted for each mirror along the optical path. This also confirms the magnification of the system as well as the astigmatism pre-correction from the cylindrical mirror which collapses the ellipse, of eccentricity $e = 0.2836$, onto a perfect circle. The cone angle is defined by the system's f/#, which matches the spectrometer f/# for all optics on the optical path. As the rays fan out and reconverge across the volume, their projection in the horizontal plane forms a triangular support, which justifies the use of the triangular kernel model for the ORF shown in Figure 16. The spectroscopy system accepts a collection cone of 0.122°, within which spatial information is inherently blurred. However, as seen in Figure 16, the width of this triangular base is about an order of magnitude smaller than the total smearing function, so its overall impact remains minor.

Shock wave motion during camera acquisition time is modelled as a trapezoidal kernel. This smearing results from the finite camera gating time during which the shock propagates across the observation window. The effective blurring width is given by the product of the shock velocity and the camera's exposure time, and therefore varies shot to shot. For the short exposure times used in the LAS test campaign, this effect remains minor, as shown in Figure 16 where the total spatial smearing is dominated by the LSF. From the FWHM, it is estimated that spectra from T6s560 have a practical spatial resolution of about 0.9 mm. This framework captures the asymmetric and space-dependent behaviour of the optics and sensor.

2. *Wavelength Calibration and Resolution*

Calibration

Precise wavelength calibration is critical to resolve absorption features. The spectral location of the laser beams must be accurately defined to target specific transitions. A gas cell containing NO at atmospheric pressure is placed along the laser's optical path, ahead of the spectrometer. The laser beams are tuned by rotating the BBO crystals to overlap the 226.149 and 226.779 nm absorption lines of NO, as shown in Figure 17. This spectrum is used to fit a wavelength axis, such that the laser emission can be matched to the pixels corresponding to the absorption lines of interest for each experiment. As the wavelength of interest are gathered around the 226.149 and 226.779 nm calibration lines, a linear fit was judged accurate enough as the wavelength interval was too small for non-linear deviation to have any significant effect. This check is carried out just before each shot, to ensure tuning of the crystals is done at a room temperature similar to the temperature at the time of the experiment.

Spectral Instrument Line Shape (ILS)

Using the most intense spectral lines on each calibration image recorded, the square root of a Voigt function [23] is fit to the signal. This was done independently for every shot, and the average experimentally measured full-width half-maximum (FWHM) parameters are 0.073 nm and 0.10 nm for Gaussian and Lorentzian profiles respectively. An example fit is shown in Figure 18.

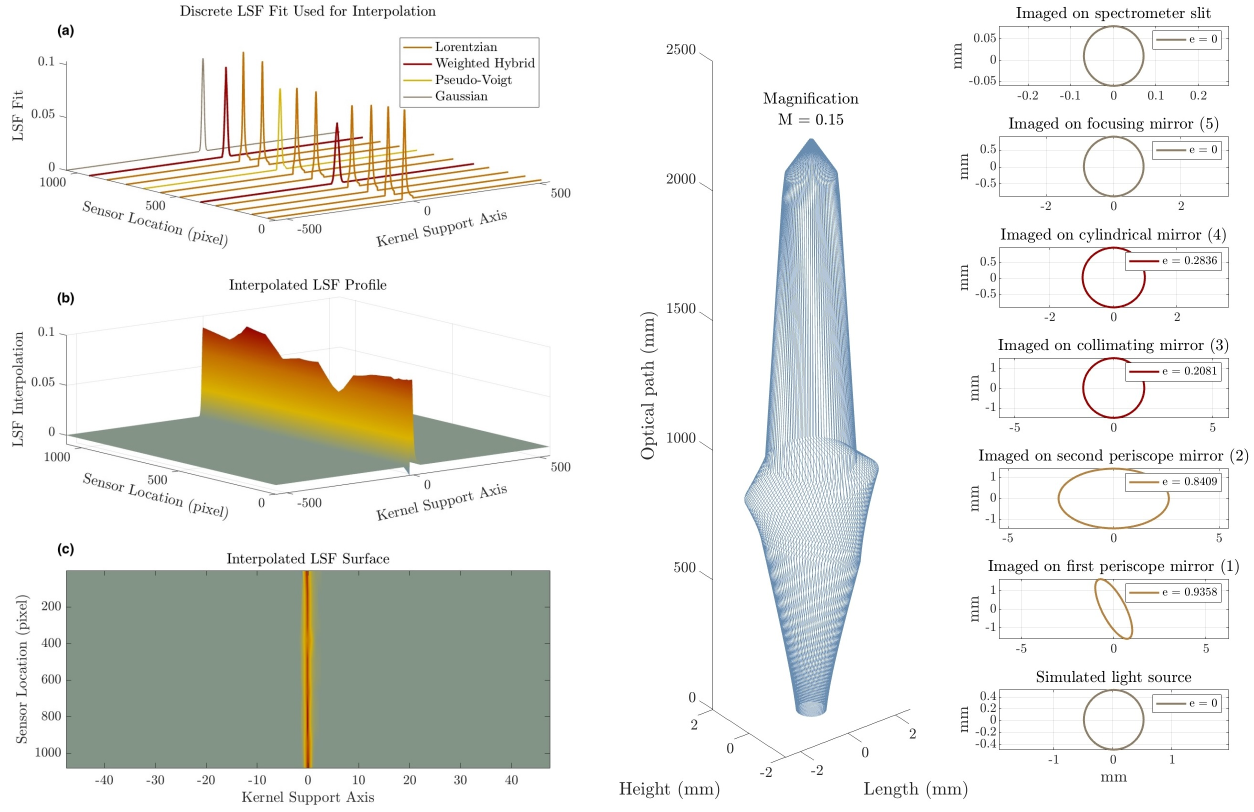

(a) Best LSF fit at the 12 locations across the sensor (top), interpolated to obtain the LSF map (middle and bottom).

(b) ORF obtained from ray-tracing simulations shown in Figure 7. Mirrors numbering is consistent between the two figures.

Fig. 15 Spatial smearing functions - LSF (left) and ORF (right).

As we are interested in absorption measurements, it was necessary to confirm the resolution of absorption features at shot conditions, where pressure varies from a third to 1.5 times atmospheric conditions, and where temperature is much higher. A deuterium (D_2) light source was set-up at the test section centerline, and the gas cell containing NO at atmospheric pressure used for wavelength calibration placed on the optical path, ahead of the spectrometer. The D_2 emission spectra was then imaged at a point in space without and with the gas cell (left and right of top of Figure 19 respectively). Absorption lines of NO at atmospheric pressure and room temperature were identified using the NO absorption spectrum generated in LIFBASE [26] at the same conditions. The instrument line shape parameters were modified in LIFBASE to match the experimentally measured absorption lines width. Once defined, these coefficients were kept constant in the empirical broadening/shift power law equation, and temperature and pressure were changed to correspond to shot conditions and obtain the resolution of our receiving optics, driving the selection of the spectrometer slit size to be kept under $10\,\mu$m to resolve finer absorption features.

Once the suitability of the optical system to measure signal from the T6 Stalker shock tube flows was confirmed and its performance characterised, absorption data could be acquired and sensibly interpreted.

IV. Experimental Procedure and Analysis

A. Flow Conditions and Laser Wavelength Selection

Three conditions were selected for the LAS campaign, presented in Table 4. Pre-campaign NESS [27]-NEQAIR [28, 29] simulations showed resolvable levels of absorption around 226 nm, and LIFBASE was used to locate temperature sensitive absorption lines. NESS-NEQAIR absorbance simulations were performed independently for NO-only, O_2-only, and all 11-species cases under Park's two-temperature formulation, with updated chemistry rates from Cruden et al. [30], to assess the contribution of each absorber to the total signal. The laser beams were then tuned to strong NO absorption lines, where O_2 absorption is negligible.

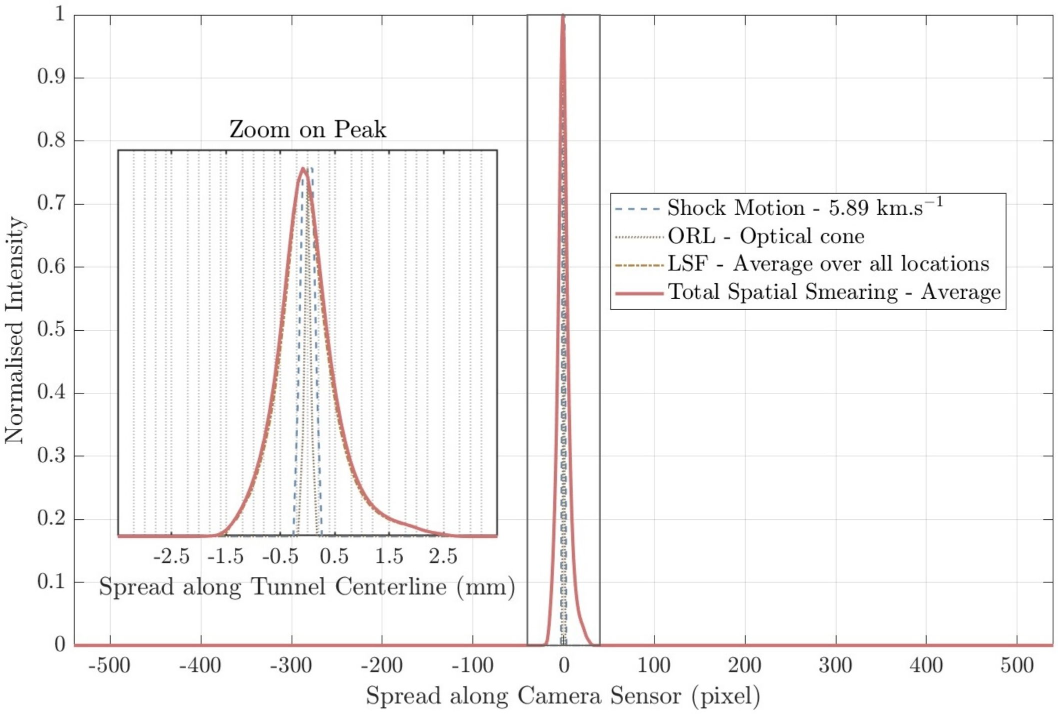

Fig. 16 **Normalised smearing functions and total SRF for T6s560.**

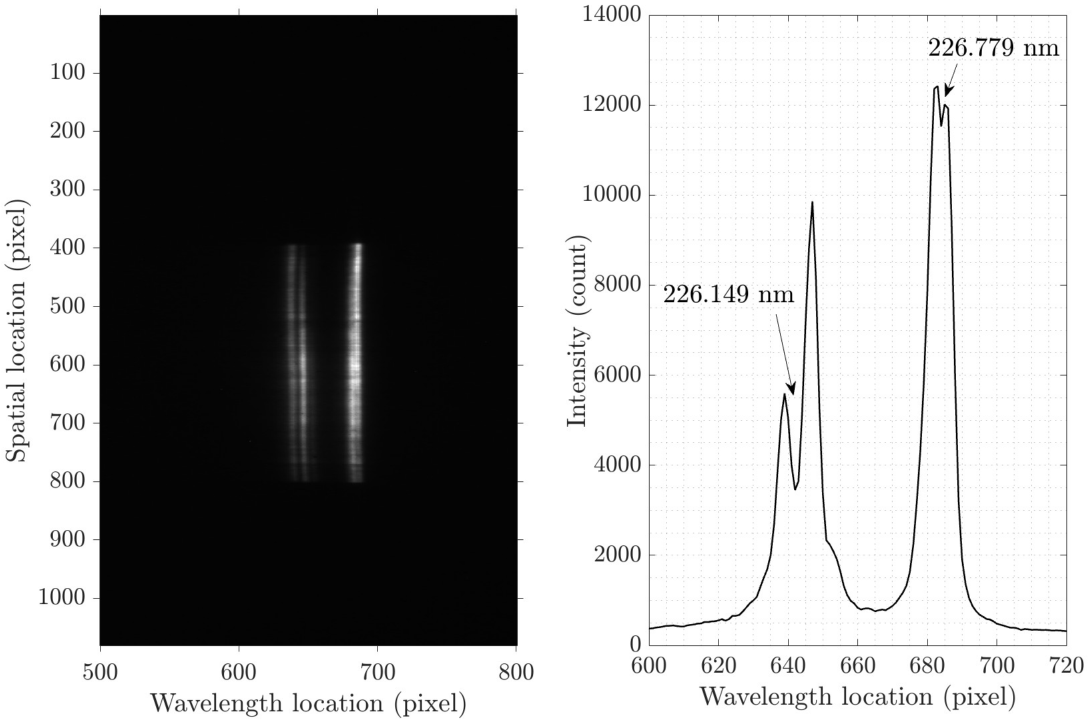

Fig. 17 **Modeless laser beams tuned on the NO gas cell absorption lines. Absorption lines of NO at 226.149 and 226.779 nm are significant at ambient conditions and are shown with the arrows.**

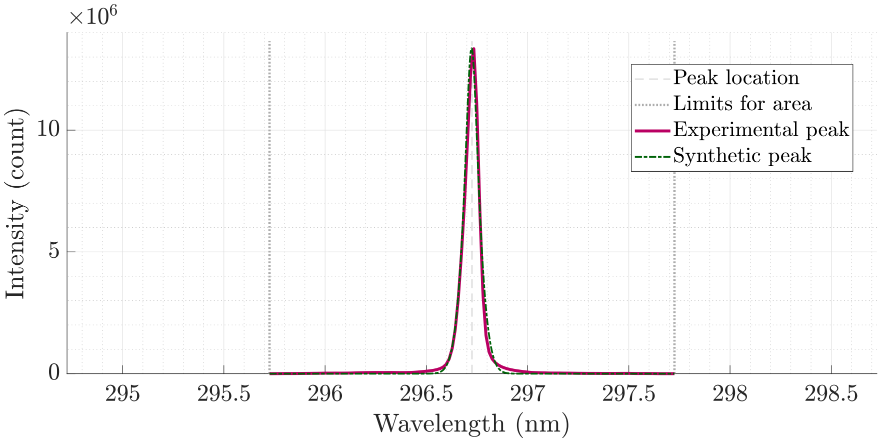

Fig. 18 ILS fitting using a synthetic lineshape to experimental measurement, for the 1200 gr.mm^{-1}

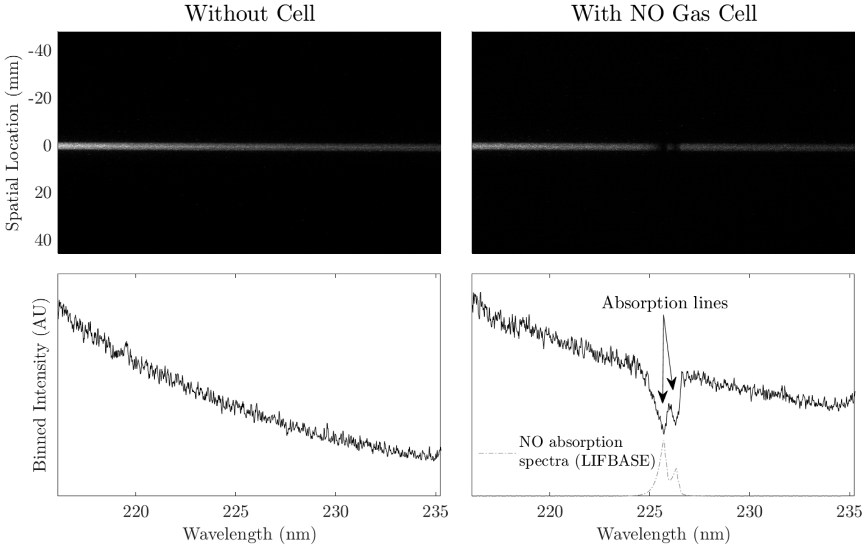

Fig. 19 D_2 emission spectra without and with an NO gas cell. Absorption lines of NO at 1 atm and 300 K appear at 226.149 and 226.779 nm.

T6s560 and T6s562 exhibit fairly similar shock speeds but mid and high post-shock pressures, guaranteeing resolvable levels of absorption through the optical path. These conditions closely recreate T6s556 and T6s553 from a previous optical emission spectroscopy (OES) campaign respectively [11, 31], such that OES-derived temperatures could be tested against simulations nominal temperatures during spectral fitting analysis [11].

Condition T6s563 was chosen to reproduce the EAST low-velocity, low-pressure regime (3–4 km.s^{-1}, 2–5 Torr) in which prior measurements reported systematic differences between NO absorption-based inferences and radiation-model predictions. Tunable diode laser absorption spectroscopy (TDLAS) showed that NO(X) absorption was broadly consistent with finite-rate predictions farther behind the shock, after the initial non-equilibrium region, while larger discrepancies appeared closer to the shock front [32]. By contrast, IR/UV emission analyses for the same freestream range indicated that equilibrium mid-IR NO is too low and that two-temperature emission fits required ~50% more NO than TDLAS at 3.81 km.s^{-1} and 2.25 Torr; UV NO bands were also underpredicted by NEQAIR [33]. By recreating this regime, T6s563 enables a like-for-like comparison between LAS-derived NO(X) number densities, finite-rate predictions, and the EAST datasets, with the aim of placing the NO trends in the current literature's context [32, 33].

Table 4 LAS Experimental test matrix. Shock tube fill pressures relate to sensor readings at the time of the shot, for ambient temperature of approximately 293 K. Beam 1 and Beam 2 give the laser beams central spectral locations.

T6s	Fill Pressure (Pa)	Shock speed ($\mathrm{km\,s^{-1}}$)	Post-shock pressure (kPa)	Beam 1 (nm)	Beam 2 (nm)
560	261.133	5.89	104.111	225.95	226.55
562	321.3	6.46	150.74	225.96	226.6
563	293	3.34	35.831	225.96	226.57

B. Calibration

To ensure the fidelity of the absorption line intensities measurements, the images obtained need careful spatial and spectral calibration, as presented in Section III. To calibrate the absorption intensity, both background and overlapping emission from the excited gas are filtered from the raw shot image, and a calibration surface is obtained using 1) a pre-shot image of the laser beam, 2) the pre-shock data from the shot image itself, and 3) the characterisation data of the beam spatial intensity distribution with gating time.

1. Background Filtering

The raw images obtained during an experiment contain the signal received by the camera from the laser beams, superimposed with a broadband background arising from camera dark current, scattered light, the emission of the post-shock gas itself, and other light sources present in the tunnel room. An example of a raw image is shown in Figure 20a for shot T6s562. This background noise, if not removed, can bias the analysis by increasing the intensity appearing to be part of the laser beam. The pre-shock section contained between the yellow dotted lines in Figure 20b is background corrected to ensure the section of the beam later used for intensity scaling is accurately measured. As the undisturbed gas is not affected by gas radiative emission, a baseline correction approach is suitable.

The bounds of the pre-shock region (yellow dotted lines in Figure 20b) are manually selected: the location of the shock can be identified by the high brightness gradient separating test section vacuum and radiating shocked gas. The laser beams' spectral locations were determined using a median spectrum of the five pixel rows at the edge of the beam. Sharp peaks along this spectrum were identified by comparing the signal to a 41-pixel moving median baseline, and the two strongest intensity deviations marked as the laser beams' centre locations. These windows were then expanded by 14 pixels on each side to include the beams' tails, and the beams temporarily replaced by a linear interpolation using the entire row to create a beam-free pre-shock region. Similar to the pedestal removal procedure outlined in Cruden et. al. [23], the 41-pixels moving median baseline routine is applied to the entire pre-shock area, this time row by row, to estimate local broadband background. The entire band is then subtracted from the original pre-shock region to obtain a beam-only image, while the post-shock region remains unchanged. Broadband removal is visible in the change from Figure 20a to Figure 20b.

2. Emission Filtering

To ensure absorption features within the laser beam spectral range are well resolved, overlapping emission from the radiating gas was filtered out. Background emission from the gas becomes more important when the laser intensity to camera gain ratio is low (i.e. for long gate times) and consequently varies from shot to shot. The correction was applied for all conditions, even when this effect was minor.

Emission from the gas was directly measured for wavelengths above and below the laser bandwidth during experiments, but the emission spectrally overlapping the laser had to be reconstructed. This corresponds to the region contained within the yellow dotted lines in Figure 20c. The emission correction is applied from this point to the end of the beams where the second dotted line is located. This corresponds to the section where emission from the gas overlaps with the absorption features of interest.

A same-frame reference spectrum created from the median of the rows 10 to 20 pixels above the edges of the beam (red dotted lines in Figure 20c) was used to provide the spectral shape. An example of a reference spectrum is shown in Figure 21a for the case of shot T6s562, which displayed the lowest laser intensity to camera gain ratio. The spectral shape is assumed uniform in space along the beam length, while its intensity varies with row. The validity of this assumption was verified using emission spectra for similar conditions obtained during the optical emission spectroscopy test campaign. Although these tests provide direct measurements of emission spectra, shot-to-shot variation led to larger changes in spectral shape than any horizontal evolution due to temperature or camera intensifier variation within the same image. This motivated the use of a reference spectrum to reconstruct emission along the beam while only using emission spectra to validate the trends.

For each row in the post-shock region, the beam locations were identified again within a 100-pixel spectral window. A local baseline was estimated using a 41-pixels moving median filter, and residuals relative to this baseline were normalised by the median absolute deviation [34, 35]. Pixels exceeding 4.5 times this robust noise scale were flagged as belonging to a beam. The resulting indices were then dilated by 14 pixels on each side to capture the full beams' width, including their tails. This per-row analysis defined the region to be reconstructed.

In contrast to background removal, a five-row median-filtered spectrum was obtained before fitting in order to suppress row-to-row noise. For each row, this filtered spectrum was formed by taking the median across the two neighbouring rows above and below. The stabilised spectral shape associated with each row Y was then fitted to the affine function in Equation 1, where X is the reference spectrum, a is a multiplicative gain accounting for camera sensor and intensifier performance variation in space as well as gas-temperature effects on the spectra, and b is an offset which corrects for background level. For each row, the constants a and b were determined using MATLAB's `robustfit` with a Huber loss regression function.

$$Y = aX + b \tag{1}$$

The original rows Y outside the bounds of the laser-beam spectral range were kept unchanged, but the constants were used with the reference spectrum to reconstruct the emission at the beam locations. The spectral structure of the X reference spectrum was injected, but the moving-median baseline of the Y row was preserved and the local noise scale of the surrounding emission used to scale the signal. A small linear adjustment ensured the filled segment met the original signal at the beam window boundaries. An example of a reconstructed background emission spectrum is shown in Figure 21d.

Finally, the reconstructed emission was subtracted from each row to obtain a laser-only spectrum. An example of a fully filtered image is shown in Figure 20c. The region between the yellow dotted lines only shows the beam and absorption features without contamination from overlapping emission background.

3. Calibration Surface

Once the shot image has been filtered to isolate the transmitted laser beams, the signal must be calibrated to quantitatively resolve absorption features. Three complementary tools are used to construct a calibration surface. First, a pre-shot image of the laser beam provides a reference intensity distribution under the same optical and room conditions as the experiment. Second, pre-shock rows from the shot image, where the laser traverses the evacuated test section without absorption, are used to scale the beams' intensities. Finally, the characterisation of the intensity distribution with gating time results are used to reconstruct the spatial beams intensity profiles to obtain a physically accurate calibration surface. This process, explained in the following section, is summarised in the chart of Figure 22.

Pre-shot Image

Immediately before each shot, the laser beam was imaged under the same dye concentration, wavelength setting, room conditions, and optical alignment as the experiment. This pre-shot image ('Pre-shot image' in Figure 22) therefore provides a raw calibration surface, representative of the beam profile in the absence of absorption.

The pre-shot image does not, however, capture the change in the beams' relative intensities nor the variation of their spatial intensity profiles caused by the cooling of the beta barium borate (BBO) crystals during the gating duration of the shot. To correct for this timing effect, the pre-shot surface must be rescaled using information from the pre-shock region of the shot image. Before this scaling, the spatial alignment of the pre-shot and shot images was verified: the maximum vertical shift required was 2 pixels, confirming that the two beam profiles are directly comparable.

Pre-shock Data

The pre-shock rows of the shot image, shown between the green dotted lines in Figure 22, were divided by the corresponding rows from pre-shot image. This produces a two-dimensional calibration factor surface, which captures the wavelength-dependent intensity change between pre-shot and shot conditions. To reduce noise, the median across rows was taken to form a one-dimensional calibration array along the wavelength axis. This array was then used to multiply all rows of the pre-shot image, yielding an intermediate scaled calibration surface that accounts for gating-time intensity variation while preserving the spectro-spatial artefacts of the pre-shot image.

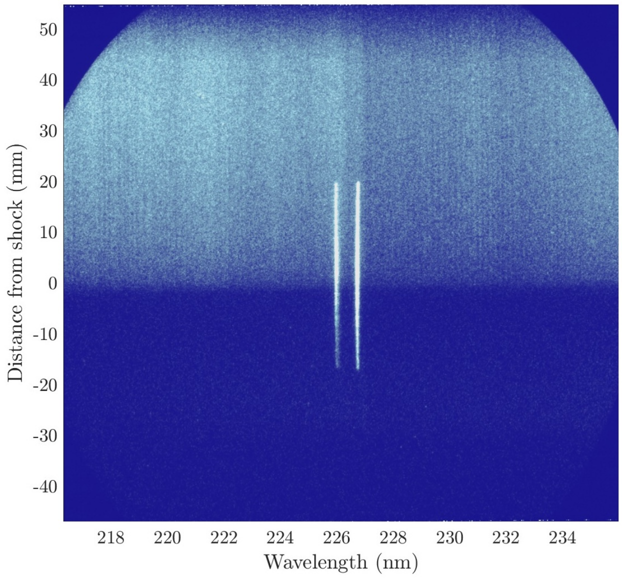

(a) Unfiltered image

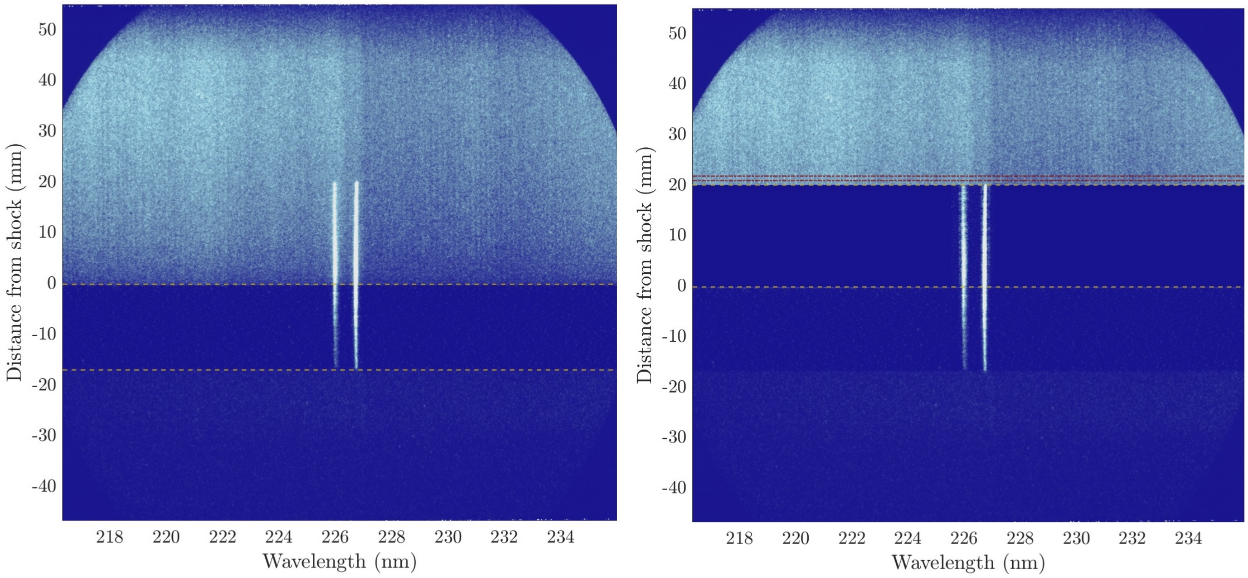

(b) Pre-shock background filtered. Correction is applied over the length of the beam unaffected by the shocked gas, between the two yellow dotted lines.

(c) Post-shock emission filtered image. Correction is applied over the length of the beam affected by the shocked gas between the two yellow dotted lines. The section between the red dotted lines is used to generate the reference spectrum from Figure 21a.

Fig. 20 Pre-shock background and post-shock emission filtering for the example of T6s562.

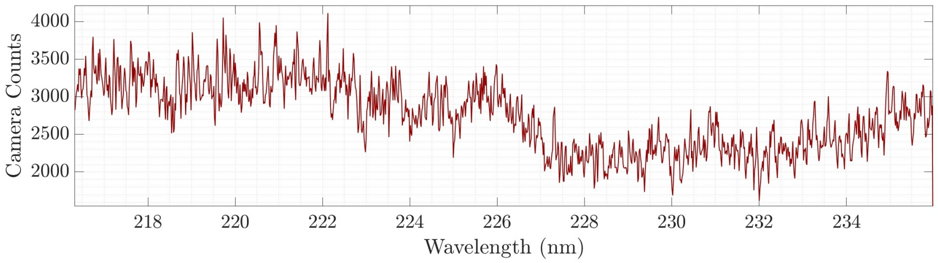

(a) Reference spectrum.

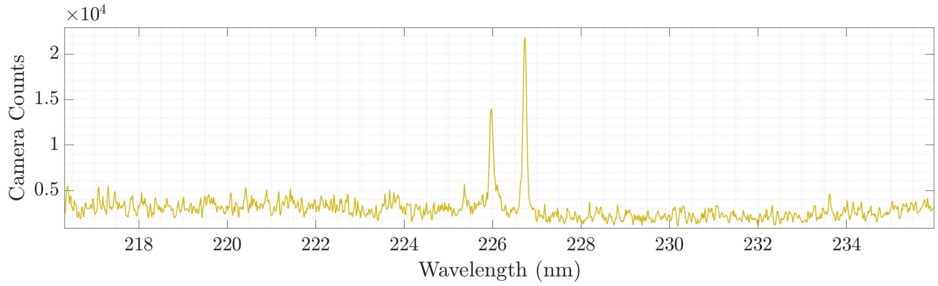

(b) Original spectrum.

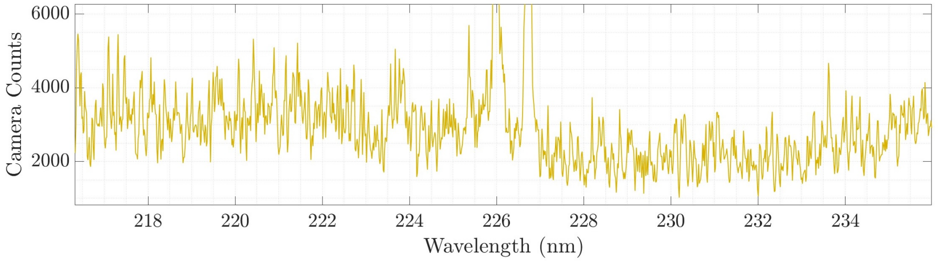

(c) Original spectrum – zoomed in.

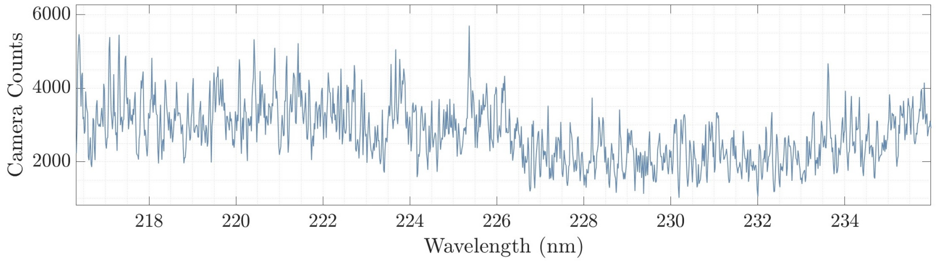

(d) Reconstructed background spectrum.

Fig. 21 Example of gas emission filtering for shot T6s562, at the middle section between the two dotted lines of Figure 20c. Only the region where the laser beams are located are spectrally reconstructed, all other wavelengths remain unchanged.

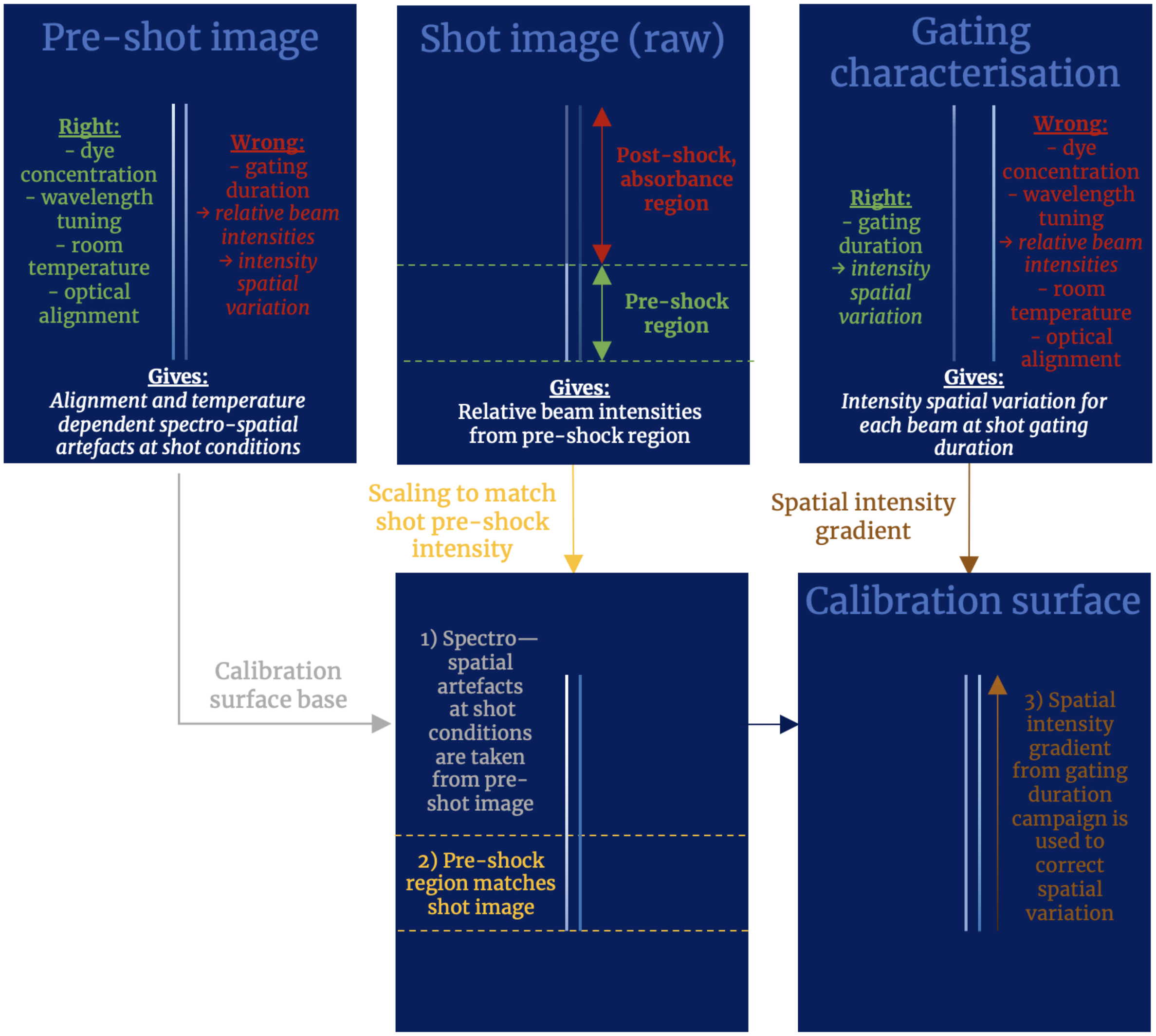

Fig. 22 Calibration surface construction chart.

Although the region of the intermediate calibration surface between the yellow dotted lines in Figure 22 matches the region between the green dotted lines of the shot image in intensity, it does not account for the spatial (vertical) variation of the beam intensity profile due to gating duration.

Spatial Scaling Using Gating Time Characterisation Campaign Data

The characterisation data presented in Figure 9 could not be directly used as a calibration surface, as the data was obtained at different wavelengths, and for different dye tuning and active molecule concentration than the shots. Rather, they were used to derive spatial variation of beam intensity with gating time.

Two complementary datasets were employed in the characterisation study. First, a photodiode placed at the exit of the modeless laser provided absolute intensity measurements down to 50 ms. For each gating time, 5 measurements were taken. This data established the global variation of laser intensity with gating time, and was linearly extrapolated below 50 ms when necessary. In particular, shot T6s560 was gated for 49.5 ms and the photodiode trend was extrapolated down to 40 ms to retrieve the trend, as shown in Figure 23a.

Second, CCD images resolved the two frequency-doubled beams individually between 250 and 2500 ms. These measurements decoupled the behaviour of the two BBO crystals, which cool at different rates, and allowed the relative as well as absolute intensity variation to be assessed. For each gating time, ten measurements were averaged to obtain the mean peak intensity of each beam shown in Figure 23b.

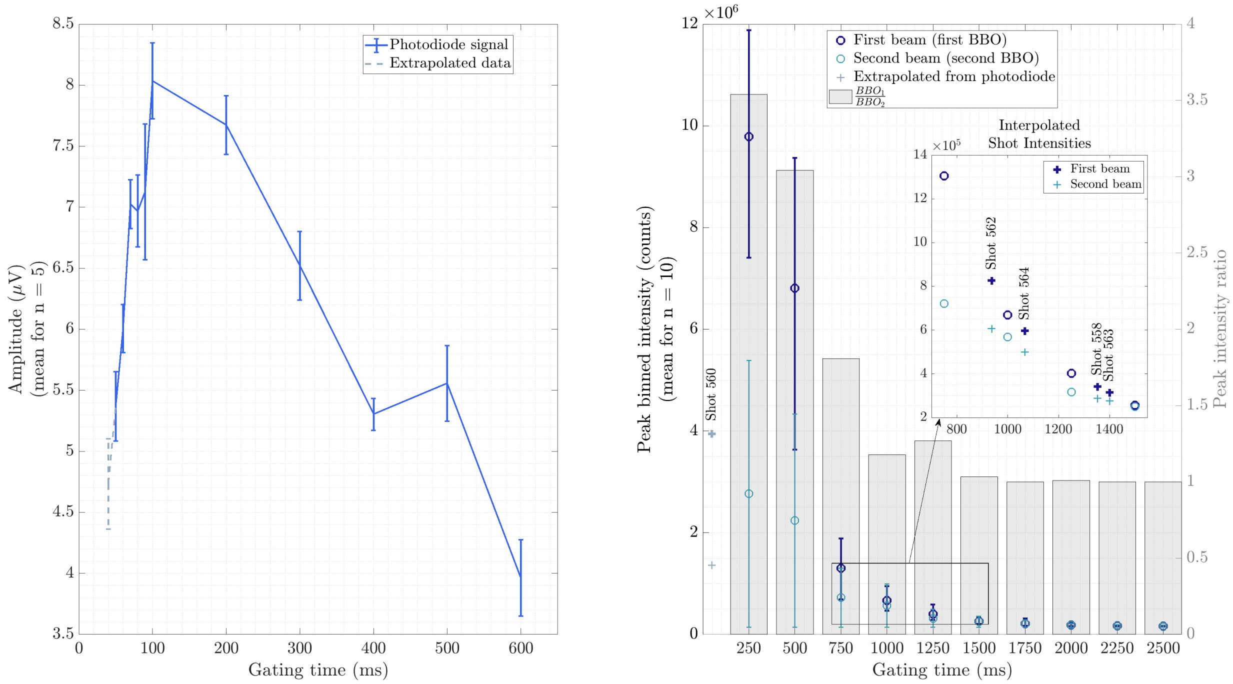

(a) Intensity recorded by a photodiode placed at the exit of the modeless laser, averaged for 5 measurements. Error bars indicate the variation across the five repeated measurements.

(b) Signal resolved by the CCD camera to differentiate the two frequency doubled beams intensity variations, averaged for 10 measurements.

Fig. 23 226 nm modeless laser intensity variation with gating times. The light blue segment in 23a and markers in 23b correspond to the extrapolation performed for shot T6s560.

The two datasets were connected by fitting a quadratic function f_1 to the photodiode trend, which was then used as a reference to extrapolate the CCD dataset. Since the photodiode and camera data are expressed in different units, their trends must be correlated. The photodiode trend f_1 was evaluated at the CCD gating times g, and an affine relation of the form Equation 2 was fitted to express the trend in camera units. This was done separately for each of the two beams, yielding coefficients (A_1, B_1) and (A_2, B_2). A coefficients account for different scaling factors between photodiode and camera signals, while B coefficients represent camera background and stray light. The resulting affine maps can then be applied to extrapolate the beam intensities for out-of-range gating times.

$$Y(g) = A f_1(g) + B \tag{2}$$

This procedure preserved the global intensity evolution observed with the photodiode, while simultaneously reproducing the relative behaviour of the two BBO beams. In this way, the CCD data was extended below 250 ms, enabling the expected beam intensities to be reconstructed for shot T6s560, as shown in Figure 23b. All other shots' gating times were concentrated between 800 and 1500 ms, and expected beam intensities were obtained by linear interpolation as shown in the inset of Figure 23b.

The reconstructed intensities with gating time were found to follow the correct overall trend when compared against the pre-shock data for the range of shots' gating times. However, the ratio of the two beams was not always reproduced with the correct orientation, although the values remained consistently close. This discrepancy is attributed to differences in dye concentration, wavelength tuning, and room temperature conditions between the dedicated characterisation campaign and the actual shot data.

Additionally to peak intensity variation, the characterisation campaign also gave information on the spatial evolution of the beam profiles with gating times. For all gating times, the trends in space were found to be highly repeatable, with peaks and dips in intensity at the same locations for all gating times and all 10 images within the same sets. However, the intensity profile was found to increase in the upper portion of the beam as gating time is decreased. As gating time increases, the distribution of intensity over space becomes more even. From these observations, the trend of the pre-shot calibration surface was kept as it captures the fine-scale spatial structure of the beam in the same optical, dye concentration and wavelength settings as the experiment. However, the intensity gradient in space for the two beams was corrected to account for gating time before applying the pre-shock region correction.

Intensity gradients across the beams were extracted from the characterisation campaign, and linearly fit to obtain the slopes for each gating time. The slopes for the two beams were then interpolated to obtain slopes at the relevant shot's gating time, which were subsequently normalised such that the shot pre-shock region remained unchanged, as shown in Figure 22. The result of this processing was that the overall scaling, fine spatial features and intensity ratio of the two beams remained dictated by the pre-shock evaluation of each individual shot, while the characterisation campaign profiles imposed the correct spatial variation expected from BBO cooling.

Calibrated surface and local transmission spectra $\mathrm{T}(\lambda, \mathrm{x})$ using this calibration surface are shown in Figure 24 for T6s562. Local spectra were obtained by averaging over rows of pixels corresponding to the full width at half maximum (FWHM) of the spatial resolution function (SRF) for the relevant shot. Data towards the wings of the beams sometimes exceeded unity after the calibration procedure. This behaviour was attributed to slight misalignment and/or beam steering within the shocked gas, which displaced the probe beams relative to the reference calibration beams that propagated through the vacuum of the test section and room atmospheric air. When the two were divided to compute the normalised transmission image (Figure 24a), these small misalignments yielded unphysical transmission values ($\mathrm{T} > 1$) near the beam edges. Consequently, pixels outside the core of the illuminated region were discarded, ensuring that only regions where transmission was physically meaningful were included in the spectral analysis. Correction using gating time data produced fewer unphysical values near the centre of the beams, with remaining artefacts concentrated toward the edges, suggesting that accounting for BBO crystal cooling provides a more accurate representation of the true transmission field.

C. Spectral Fitting

Full spatial field (including shock front and non-equilibrium region) thermochemistry is modelled using the Oxford University's Non-Equilibrium Shock Solver (NESS) [27]. The equilibrated thermochemical state is modelled using NASA's Chemical Equilibrium with Applications (CEA) at the same conditions, as well as for the temperatures obtained from the optical emission spectroscopy (OES) spectral fitting routines.

The outputs from the thermochemistry solvers are provided to NASA's Nonequilibrium Air Radiation (NEQAIR v15.1) program [28, 29], to compute local spectral absorption coefficients (cm^{-1}). These simulated coefficients are then fit to experimental data to evaluate how the NO number densities n_{NO} deviate from the NESS and CEA-predicted thermochemistry at the reconstructed shot conditions, as well as from the CEA-derived gas composition for T_{tr} using the OES campaign best-fit temperatures.

The spectral absorbance $\mathrm{A}(\lambda, \mathrm{x})$ was computed from the calibrated transmission spectra $\mathrm{T}(\lambda, \mathrm{x})$ using the Beer-Lambert law (Equation 3) with the known optical path length L (T6 Stalker shock tube diameter, 22.5 cm) through the absorbing gas, to obtain local absorption coefficients in units of cm^{-1}, consistent with the NEQAIR simulations.

$$\mathrm{A}(\lambda, \mathrm{x}) = -\frac{\ln(\mathrm{T}(\lambda, \mathrm{x}))}{\mathrm{L}} \tag{3}$$

The simulated absorption spectra $\mathrm{A}_{\mathrm{sim}}(\lambda)$ (for NO, O_2, and all 11 air species combined) were then convolved to the experimental spectral resolution function and interpolated onto the experimental wavelength grid. As the fitting results from optical emission spectroscopy campaign did not allow to identify clearly a vibrational temperature T_v nor confirm equilibrium, a scaling approach was adopted to quantify NO number density agreement between experiment and simulation. To do so, a scalar multiplicative factor s was determined at different post-shock locations by minimising the least-squares difference between measured and simulated absorbance spectra (Equation 4).

$$\min_{s} \left\| \mathrm{A}_{\mathrm{exp}}(\lambda, \mathrm{x}) - s\, \mathrm{A}_{\mathrm{sim}}(\lambda, \mathrm{x}) \right\|_2^2 \tag{4}$$

The scaling factor s represents the multiplicative correction required to align the simulated absorbance with experimental data. Since the simulated absorbance scales linearly with the number density of the absorbing species, the value of s provides a direct estimate of the NO number density correction (Equation 5), as long as the spectral region used for the scaling is not contaminated by absorption from other species.

$$n_{\mathrm{NO,\,exp}} \approx s\, n_{\mathrm{NO,\,sim}} \tag{5}$$

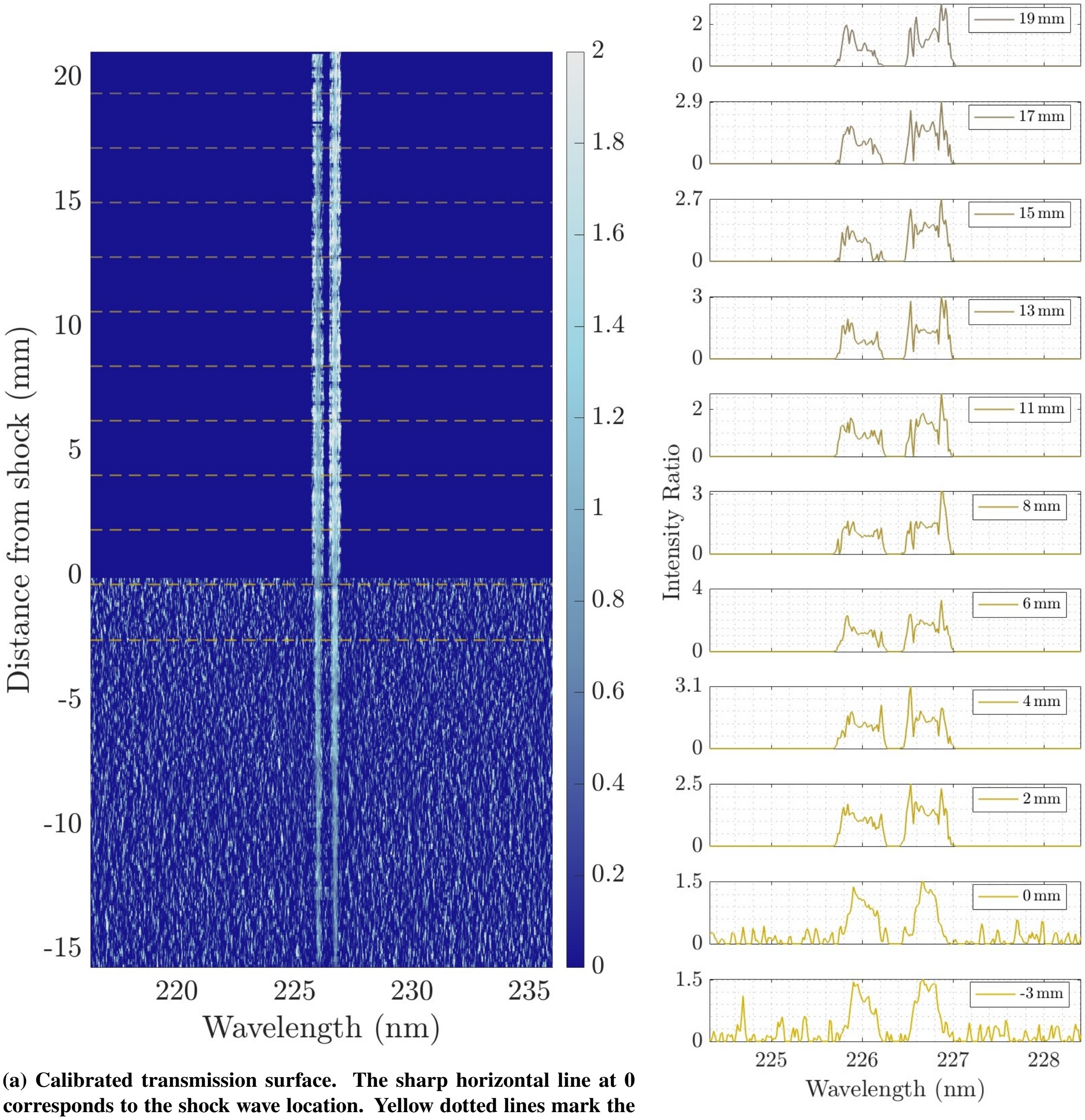

(a) Calibrated transmission surface. The sharp horizontal line at 0 corresponds to the shock wave location. Yellow dotted lines mark the spatial locations of the spectra shown in Figure 24b. False colour indicates transmission according to colour bar.

(b) Transmission spectra T(λ, x) at the locations shown by the dotted lines in 24a.

Fig. 24 Example of processed LAS transmission T(λ, x) data for shot T6s562. This injects the spatial evolution of the intensity profile from the gating time experiments onto the pre-shock data. The bottom two spectra corresponds to pre-shock beam emission, while the evolution of the absorption features behind the shock wave can be observed downstream. Spatial resolution function (SRF) FWHM is of 10 pixels, and instrument line shape (ILS) FWHM of 5 pixels. Values above unity are calibration artefacts and are discarded during data processing.

Thus, $s > 1$ indicates that the simulation underpredicts NO absorption (and number density n_{NO}), while $s < 1$ implies an overprediction. Examples of spectral fits are shown in Figure 25 for different discrete locations, with scaled simulations in grey.

The scaling analysis was performed independently for the NO-only, O_2-only (relevant for T6s563, Figure 25c), and all 11-species from the thermochemical air model synthetic spectra to assess the contribution of each absorber to the total signal. However, the spectral regions targeted by the laser corresponded to strong NO absorption lines, where O_2 absorption is negligible even in the case of T6s553, as shown in Figure 25c where the 11-species and NO-only spectra overlap. As a result, the experimental spectra are effectively NO-dominated, and the derived scaling factor s primarily reflects deviations in the predicted NO number density rather than cross-species or background effects.

V. Results and Discussion

These experiments aim at broadening the understanding of high-speed shock tubes thermochemistry, by bringing spatially resolved absorption data within one image while relying on a single laser pulse. The data presented in this section serves as a proof of concept for the modeless laser capability to produce such measurements, which would complement optical emission spectroscopy (OES) at the same conditions. Where OES can probe high energy states, LAS provides information about the low-lying states from which rotational temperatures T_r and NO number densities n_{NO} can be inferred. While OES requires meticulous spectral radiance calibration, LAS can be calibrated using the laser pulse directly.

Previous experimental studies of NO absorption in high-enthalpy flows have revealed notable discrepancies between measured spectra and predictions from equilibrium and non-equilibrium thermochemical models [33, 36]. These inconsistencies highlight ongoing uncertainty in NO population distributions and absorption behaviour. Acquiring high-fidelity datasets is therefore essential to constrain model assumptions, improve predictive capability, and resolve the disagreements reported in the literature.

Table 5 Temperatures (in K) used as inputs to NEQAIR simulations for each shot. T6s563 NESS temperature is shown as $\sim T_{eq}$, as equilibrium is not fully reached in the simulation at the post-shock locations shown in the subsequent figures and analysis.

T6s	T_{eq} NESS	T_{eq} CEA
560	6279	6298
562	6727	6749
563	~3487	3365

The LAS results presented in this section demonstrate that a single modeless laser pulse can provide spatially resolved post-shock absorption measurements, enabling direct comparison with NEQAIR predictions at multiple downstream locations. Because the OES campaign did not reliably constrain vibrational temperatures or confirm equilibrium farther behind the shock, the analysis does not focus on extracting precise trans-rotational temperatures and NO number densities. Instead, OES-derived temperatures were used to test whether they produce improved agreement with LAS when used as inputs to CEA-NEQAIR simulations. These results are discussed in related publications [11].

The scaling factors required to match NEQAIR simulations to experiment are shown in Figure 26, and the corresponding inferred number densities are plotted in Figure 27. The temperatures used as inputs for all simulation models can be found in Table 5. Across all three conditions, a clear global trend emerges: NEQAIR underpredicts NO immediately behind the shock, with scaling factors $s > 1$ over the first 10-15 mm. At higher post-shock pressure (T6s562), this underprediction persists over the full measurement range, while at lower pressure (T6s560 and T6s563), a downstream crossover appears where $s < 1$ and the simulations exceed experiment.

Kinetically, the observed behaviour is consistent with results reported in prior studies in the EAST facility [33, 36]. Underprediction near the shock indicates insufficient production of NO through the Zel'dovich exchange reactions,

$$N + O_2 \rightleftharpoons NO + O, \qquad O + N_2 \rightleftharpoons NO + N,$$

implying a modeled deficit of N and O atoms and/or slightly low post-shock translational temperatures.

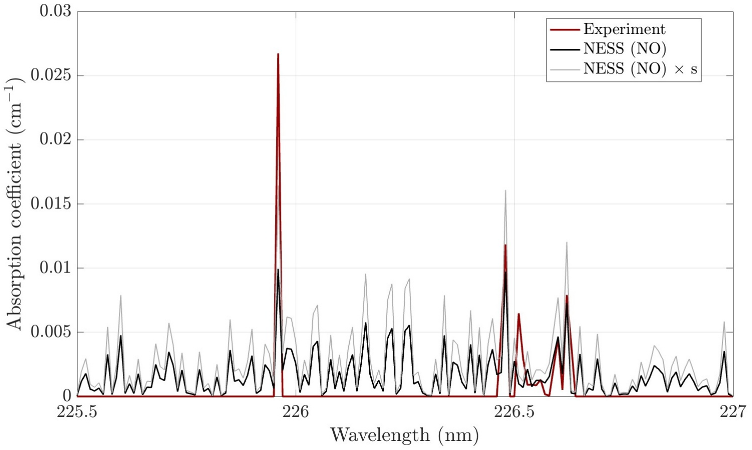

(a) T6s560: 5.9 km.s^{-1}, 104 kPa. 14 mm post-shock. s = 1.65; absorbance is underpredicted by NESS-NEQAIR up to about 15 mm.

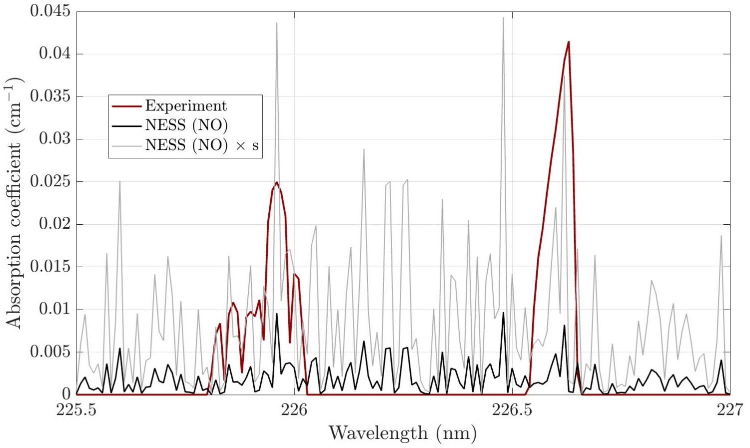

(b) T6s562: 6.5 km.s^{-1}, 150 kPa. 18 mm post-shock. s = 4.56; absorbance is underpredicted by NESS-NEQAIR at all locations.

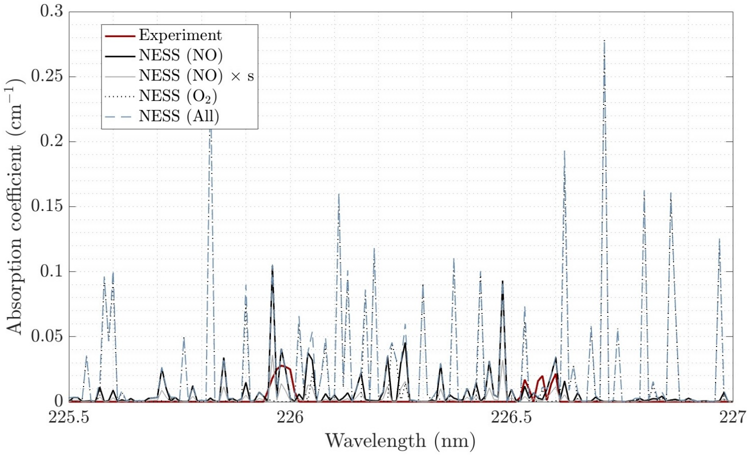

(c) T6s563: 3.3 km.s^{-1}, 35.8 kPa. 21 mm post-shock. s = 0.34; absorbance is overpredicted by NESS-NEQAIR up to about 16 mm.

Fig. 25 Examples of simulated VS experimental spectra and required scaling factors.

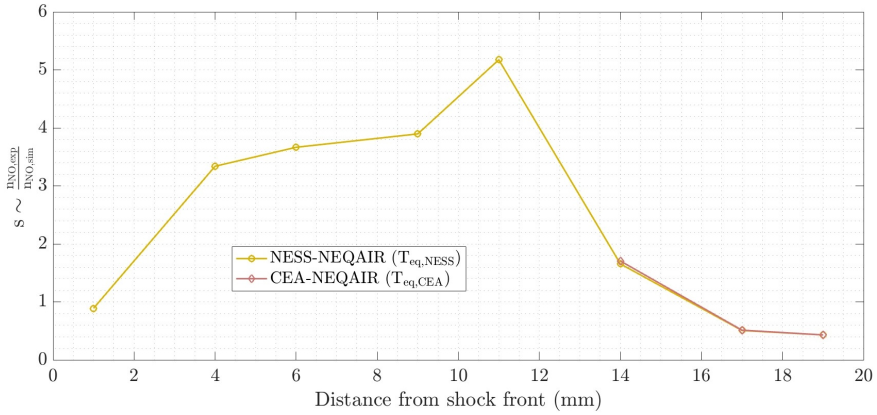

(a) T6s560: 5.9 km.s^{-1}, 104 kPa. Absorbance is underpredicted by NESS-NEQAIR and CEA-NEQAIR up to about 15 mm post-shock, and at all locations using the temperatures from OES best fit.

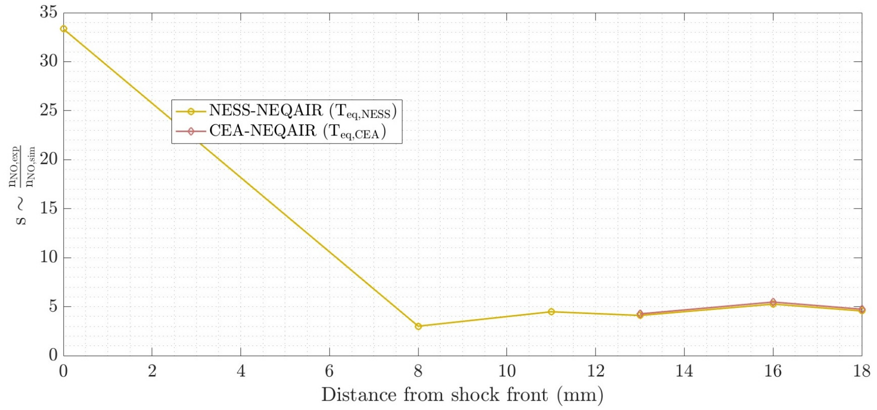

(b) T6s562: 6.5 km.s^{-1}, 150 kPa. Absorbance is underpredicted by NESS- and CEA-NEQAIR, and overpredicted using the temperatures from OES trend best fit. NEQAIR simulations based on OES trend best fit temperatures agree closely with experiment ($s \approx 1$).

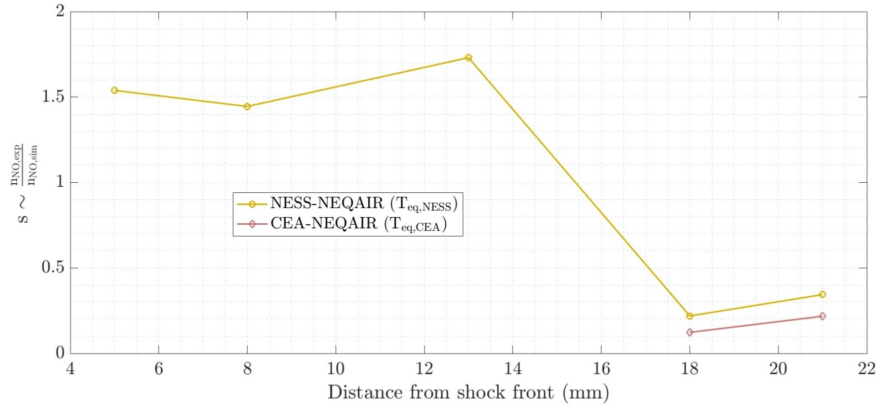

(c) T6s563: 3.3 km.s^{-1}, 35.8 kPa. Absorbance is underpredicted by NESS-NEQAIR up to about 14 mm post-shock, and overpredicted by CEA-NEQAIR at all locations.

Fig. 26 Scaling factors for different post-shock locations. The temperatures used to generate the NEQAIR simulations can be found in Table 5.

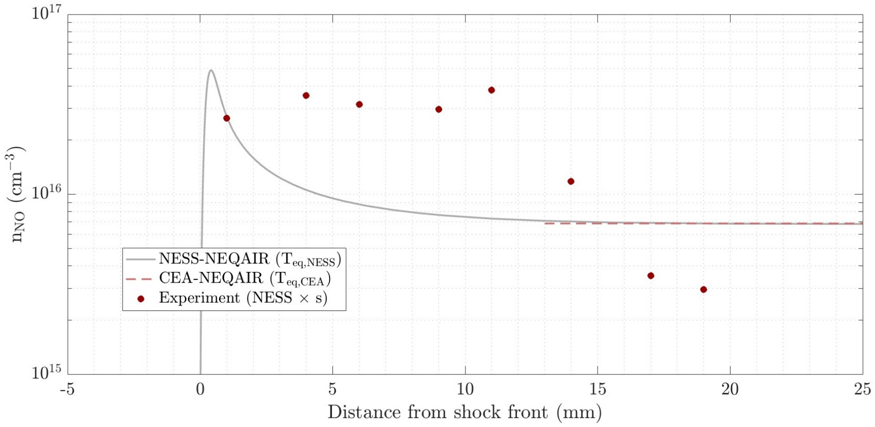

(a) T6s560: 5.9 km.s^{-1}, 104 kPa. n_{NO} are underpredicted by NESS-NEQAIR and CEA-NEQAIR up to about 15 mm post-shock, and at all locations using the temperatures from OES best fit.

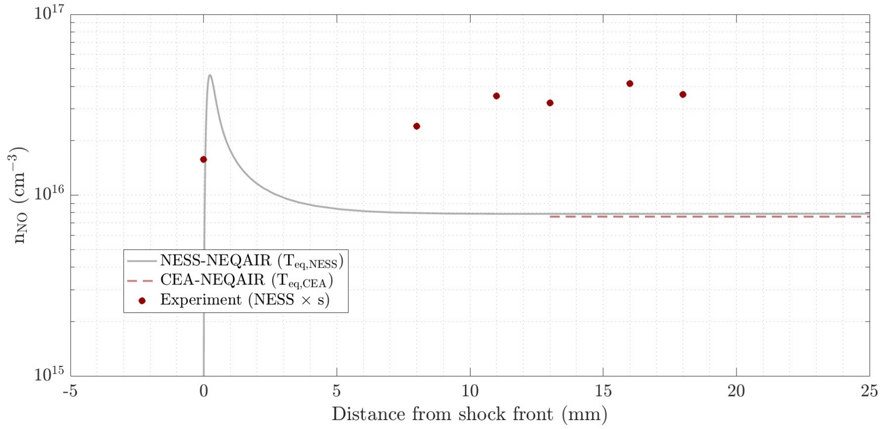

(b) T6s562: 6.5 km.s^{-1}, 150 kPa. n_{NO} are underpredicted by NESS- and CEA-NEQAIR, and overpredicted using the temperatures from OES trend best fit. NEQAIR simulations based on OES trend best fit temperatures agree closely with experiment ($s \approx 1$ - note the logarithmic scale).

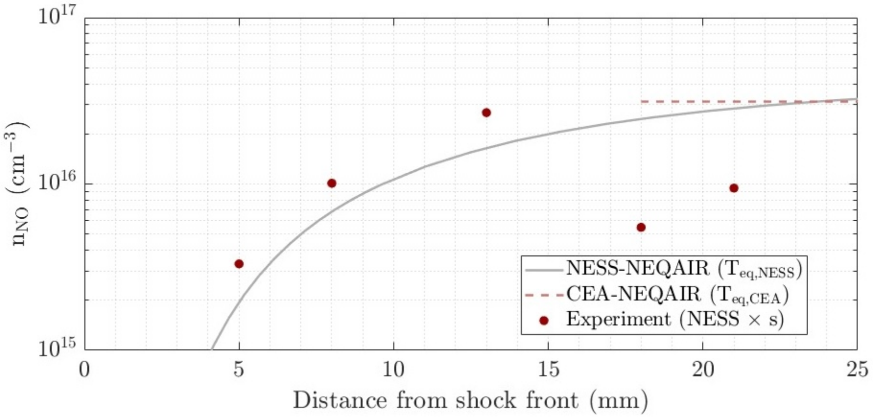

(c) T6s563: 3.3 km.s^{-1}, 35.8 kPa. n_{NO} are underpredicted by NESS-NEQAIR up to about 14 mm post-shock, and overpredicted by CEA-NEQAIR at all locations.

Fig. 27 NO number densities for different post-shock locations. The temperatures used to generate the NEQAIR simulations can be found in Table 5.

Downstream, the crossover in the lower-pressure cases indicates that NO is destroyed too slowly in the simulations through

$$NO + O \rightleftharpoons N + O_2, \qquad NO + M \rightleftharpoons N + O + M.$$

Thus, finite-rate models appear to lag the experiment both in formation of NO immediately behind the shock, and in removal of NO farther downstream.

Although the same physical trend appears throughout all three conditions, the magnitude and downstream evolution differ with pressure and shock speed. For T6s560 (5.9 km.s^{-1}, 104 kPa), the scaling factor remains above unity for roughly the first 15 mm behind the shock before crossing below one, and the inferred NO number densities predominantly fall in the low-10^{16} cm^{-3} range. In the highest-pressure case, T6s562 (6.5 km.s^{-1}, 150 kPa), s remains between approximately 3 and 5.5 over the entire measurement range, with no downstream crossover. Faster thermal and chemical relaxation at this pressure reduces the spatial extent of non-equilibrium, but the underprediction of NO persists, with number densities again on the order of 10^{16} cm^{-3}. At the lowest-pressure condition, T6s563 (3.3 km.s^{-1}, 35.8 kPa), the overshoot and relaxation behaviours are still present but with reduced magnitudes. The inferred NO number densities fall in the mid-10^{15} cm^{-3} to low-10^{16} cm^{-3} range (Figure 27c), rising rapidly behind the shock and relaxing further downstream. Although the absolute densities are lower than the EAST TDLAS measurements of Chang et al. at 3.81 km.s^{-1} and 2.25 Torr, which scatter around $3–5 \times 10^{16}$ and relax toward finite-rate predictions farther downstream [36], the qualitative behaviour is similar to the results reported. Compared with the emission-based reconstruction of Cruden et al. at the same freestream condition, which shows a larger early overshoot of $6–8 \times 10^{16}$ cm^{-3} [33], T6s563 shows a more moderate deviation from equilibrium predictions. Although the T6s563 profile is reported over a shorter distance than the EAST profile, both datasets show an NO overshoot followed by a decrease toward equilibrium downstream of the shock.

VI. Conclusion

This paper presents the newly developed laser absorption spectroscopy setup of the Oxford University Thermofluids Institute. Laser absorption spectroscopy (LAS) was introduced as a complementary diagnostic to the VUV OES set-up developed and used during a previous test campaign on the same experimental conditions, enabling direct measurement of NO number density behind strong shocks in T6. A calibration methodology was developed to recover spatially resolved transmission images from a single modeless laser pulse, allowing comparison with NEQAIR at multiple post-shock locations.

Across all three cases, NEQAIR underpredicted NO immediately behind the shock ($s > 1$), consistent with the OES observation that discrepancies originate in NO-dominated spectral regions. At lower pressure, the error diminished downstream and reversed sign, while it persisted at higher pressure.

LAS therefore removes a key population-composition ambiguity present in OES-only analysis, and the combined diagnostics demonstrated that current finite-rate models underpredict early NO formation and overpredict its downstream persistence.

The dataset acquired in this thesis contains significantly more information than was extracted in the first round of analysis, and several avenues exist to retrieve additional thermochemical insight from the same measurements.

The LAS measurements obtained here provide a fully spatially resolved map of the absorption field, even though only discrete spectra were analysed in this thesis. A more complete spatial reconstruction of n_{NO} could be performed by fitting the full set of spectra along the shock-normal direction, yielding a higher-resolution recovery of the NO overshoot, relaxation behaviour, and post-shock equilibration. In addition, the selected temperature-sensitive line pairs enable ratio-based thermometry, such that vibrational and rotational temperature could be inferred where absorption SNR permits.

Finally, the combined OES and LAS dataset is well suited for inversion frameworks that enforce mass, energy and charge conservation. In particular, the conservation-law constrained fitting approach developed by Glenn [31] provides a natural pathway to jointly retrieve temperature and species populations from both diagnostics simultaneously. Applying such a framework to the present dataset would remove the remaining degrees of freedom in the reconstruction and deliver a fully self-consistent state profile throughout the relaxation region, providing a high-quality validation target for finite-rate kinetic models.

Acknowledgments

This research was funded in whole by the UKRI Future Leaders Fellowship scheme (grant number MR/T041269/1) and we extend our gratitude to UKRI. For the purpose of Open Access, the author has applied a CC BY public copyright licence to any Author Accepted Manuscript (AAM) version arising from this submission.

References

[1] Cruden, B. A., and Brandis, A. M., "Measurement of Radiative Non-equilibrium for Air Shocks Between 7-9 km/s," American Institute of Aeronautics and Astronautics, 2017. https://doi.org/10.2514/6.2017-4535.

[2] Cruden, B., Martinez, R., Grinstead, J., and Olejniczak, J., "Simultaneous Vacuum-Ultraviolet Through Near-IR Absolute Radiation Measurement with Spatiotemporal Resolution in An Electric Arc Shock Tube," American Institute of Aeronautics and Astronautics, 2009. https://doi.org/10.2514/6.2009-4240.

[3] YAMADA, G., KAJINO, M., and OHTANI, K., "Experimental and numerical study on radiating shock tube flows for spacecraft reentry flights," *Journal of Fluid Science and Technology*, Vol. 14, 2019, pp. JFST0022–JFST0022. https://doi.org/10.1299/jfst.2019jfst0022.

[4] Silva, M. L. D., Ferreira, R., Rodrigues, R., Alves, L., Gonçalves, B., Smith, A., Merrifield, J., Villace, V., and Marraffa, L., "Qualification of the European Shock-Tube for High Enthalpy Research," American Institute of Aeronautics and Astronautics, 2020. https://doi.org/10.2514/6.2020-0624.

[5] Kozlov, P. V., Levashov, V. Y., Gerasimov, G. Y., Zabelinskii, I. E., and Bykova, N. G., "Study of Radiation Characteristics of Shock-Heated Gases," *Journal of Engineering Physics and Thermophysics*, Vol. 96, 2023, pp. 1828–1838. https://doi.org/10.1007/s10891-023-02852-4.

[6] Clarke, J., Mare, L. D., and McGilvray, M., "Spatial Transformations for Reacting Gas Shock Tube Experiments," *AIAA Journal*, Vol. 61, 2023, pp. 3365–3374. https://doi.org/10.2514/1.J062604.

[7] Satchell, M., Mare, L. D., and McGilvray, M., "Flow Nonuniformities Behind Accelerating and Decelerating Shock Waves in Shock Tubes," *AIAA Journal*, Vol. 60, 2022, pp. 1537–1548. https://doi.org/10.2514/1.J060375.

[8] Collen, P. L., Satchell, M., Mare, L. D., and McGilvray, M., "The influence of shock speed variation on radiation and thermochemistry experiments in shock tubes," *Journal of Fluid Mechanics*, Vol. 948, 2022, p. A51. https://doi.org/10.1017/jfm.2022.727.

[9] Streicher, J. W., Krish, A., Wang, S., Davidson, D. F., and Hanson, R. K., "Measurements of Oxygen Vibrational Relaxation and Dissociation Using Ultraviolet Laser Absorption in Shock Tube Experiments," American Institute of Aeronautics and Astronautics, 2019. https://doi.org/10.2514/6.2019-0795.

[10] Gilvey, J. J., Goldenstein, C. S., Downing, C., Lyon, B. T., Lynch, K. P., and Wagner, J. L., "Characterization of Non-Equilibrium NO in Hypersonic Air via Laser Absorption Spectroscopy," American Institute of Aeronautics and Astronautics, 2024. https://doi.org/10.2514/6.2024-2832.

[11] Buquet, M., "Optical Diagnostics for Nitric Oxide in High-Temperature Shock Tube Flows," 2025.

[12] Collen, P., Doherty, L. J., Subiah, S. D., Sopek, T., Jahn, I., Gildfind, D., Geraets, R. P., Gollan, R., Hambidge, C., Morgan, R., and McGilvray, M., "Development and commissioning of the T6 Stalker Tunnel," *Experiments in Fluids*, Vol. 62, 2021, p. 225. https://doi.org/10.1007/s00348-021-03298-1.

[13] Glenn, A. B., Collen, P. L., and McGilvray, M., "Experimental Non-Equilibrium Radiation Measurements for Low-Earth Orbit Return," American Institute of Aeronautics and Astronautics, 2022. https://doi.org/10.2514/6.2022-2154.

[14] McGilvray, M., Collen, P., Doherty, L., Steer, J., Leader, J., Glenn, A., and Hambidge, C., "The Oxford T6 Stalker tunnel: performance, upgrades and new modes of operation," European Space Agency, 2022.

[15] Hermann, T., Collen, P., Glenn, A., Sopek, T., McGilvray, M., and Mare, L. D., "Emission spectroscopy of low density air shock tube flows above 10 km/s," European Space Agency, 2022.

[16] Ewart, P., "A modeless, variable bandwidth, tunable laser," *Optics Communications*, Vol. 55, 1985, pp. 124–126. https://doi.org/10.1016/0030-4018(85)90314-1.

[17] Snowdon, P., Skippon, S. M., and Ewart, P., "Improved precision of single-shot temperature measurements by broadband CARS by use of a modeless laser," *Applied Optics*, Vol. 30, 1991, p. 1008. https://doi.org/10.1364/AO.30.001008.

[18] Ewart, P., Arita, Y., Bultitude, K., Richard, K., and Manson, P., "Modes for Molecules : Lasers for Optical Diagnostics of Combustion," 2005. URL https://api.semanticscholar.org/CorpusID:53696819.

[19] Kaminski, C. F., and Ewart, P., "Multiplex H2 coherent anti-Stokes Ramanscattering thermometry with a modeless laser," *Appl. Opt.*, Vol. 36, 1997, pp. 731–734. https://doi.org/10.1364/AO.36.000731, URL https://opg.optica.org/ao/abstract.cfm?URI=ao-36-3-731.

[20] Buquet, M., Glenn, A., Collen, P., Williams, B., McGlivray, M., and Hermann, T. B., "DESIGN OF A SPATIALLY RESOLVED VUV SPECTROSCOPY SYSTEM FOR SHOCK TUBE FLOWS," European Space Agnecy, 2022.

[21] Buquet, M. T., Chang, E. W. K., Williams, B. A., and Hermann, T., "Experimental Characterization of a Small Scale Arc-Jet Flow Using a Spatially Resolved UV-nIR Spectroscopy System," American Institute of Aeronautics and Astronautics, 2024. https://doi.org/10.2514/6.2024-2212.

[22] Brett, B. A. C., "UPDATES TO THE NEQAIR RADIATION SOLVER," 2014.

[23] Cruden, B., "Absolute Radiation Measurements in Earth and Mars Entry Conditions," *Radiation and Gas-surface Interaction Phenomena in High-speed Reentry Lecture Series*, 2014.

[24] Yury, "https://github.com/caiuspetronius/Optometrika, GitHub," *Optometrika Library*, 2002.

[25] Cruden, B. A., "Electron Density Measurement in Reentry Shocks for Lunar Return," *Journal of Thermophysics and Heat Transfer*, Vol. 26, 2012.

[26] Luque, J., "LIFBASE 2.1 program," 2022.

[27] Clarke, J., Brody, S., Steer, J., McGilvray, M., and di Mare, L., "Quasi-one-dimensional non-equilibrium method for shock tube and stagnation line flows," , 2024. https://doi.org/10.1063/5.0218676.

[28] Parl, C., "Nonequilibrium Air Radiation (NEQAIR) Program: User's Manual," *NASA Technical Memorandum*, , No. 86707, 1985.

[29] Brandis, A. M., and Cruden, B. A., "NEQAIR v15.0 Release Notes, Nonequilibrium and Equilibrium Radiative Transport and Spectra Program," , No. 86707, 1985.

[30] Cruden, B. A., and Brandis, A. M., *Measurement of Radiative Non-equilibrium for Air Shocks Between 7-9 km/s*, 2017. https://doi.org/10.2514/6.2017-4535, URL https://arc.aiaa.org/doi/abs/10.2514/6.2017-4535.

[31] Glenn, A. B., "Fundamental non-equilibrium experiments relevant to low earth orbit return missions," Ph.D. thesis, 2025.

[32] Chang, E. W. K., Joglekar, C., McGilvray, M., and Hermann, T., "Integration of Arc-jet in Impulse Facility for Hypervelocity Aerothermal Testing with Ablation," American Institute of Aeronautics and Astronautics, 2023. https://doi.org/10.2514/6.2023-2334.

[33] Cruden, B., "Radiative Emission in Incident Air Shocks From 3–7 km/s," 2024. https://doi.org/10.2514/6.2024-3653.

[34] National Institute of Standards and Technology (NIST), "Median Absolute Deviation," *Statistical Engineering Division*, 2016. URL https://www.itl.nist.gov/div898/software/dataplot/refman2/auxillar/mad.htm.

[35] Rousseeuw, P. J., and Croux, C., "Alternatives to the Median Absolute Deviation," *Journal of the American Statistical Association*, Vol. 88, No. 424, 1993, pp. 1273–1283. URL http://www.jstor.org/stable/2291267.

[36] Chang, J. E., Strand, C. L., Hanson, R. K., Tibere-Inglesse, A. C., and Cruden, B. A., "Rapid-Scanning Tunable Laser Absorption Measurements of Shock-Heated Nonequilibrium Air Species in the NASA Electric Arc Shock Tube," *International Symposium on Shock Waves*, 2023.